


















# The GALAH Survey: Neutron-Capture Elemental Abundances for 350,000 *Gaia*-RVS Spectra and the Chemodynamics of Accreted Structures

Pradosh Barun Das <sup>1,2,3</sup>\* Daniel B. Zucker <sup>1,2</sup> Aldo Mura-Guzmán <sup>1,2</sup> Nicholas W. Borsato <sup>1,2,4</sup>  
 Gayandhi M. De Silva <sup>1,2,5</sup> Sven Buder <sup>5,6</sup> Diane Feuillet <sup>7,8</sup> Thomas Nordlander <sup>9</sup>  
 Melissa K. Ness <sup>5</sup> Sarah L. Martell <sup>10</sup> Janez Kos <sup>11</sup> Joss Bland-Hawthorn <sup>12</sup> Ken C. Freeman <sup>5</sup>  
 Andrew R. Casey <sup>13,14</sup> Geraint F. Lewis <sup>12</sup> Dennis Stello <sup>10,12</sup> Richard de Grijs <sup>1,2,15</sup>  
 and the GALAH Collaboration<sup>†</sup>

<sup>1</sup>*School of Mathematical and Physical Sciences, Macquarie University, Sydney, NSW 2109, Australia*

<sup>2</sup>*Astrophysics and Space Technologies Research Centre, Macquarie University, Sydney, NSW 2109, Australia*

<sup>3</sup>*European Southern Observatory, Karl-Schwarzschild-Str.2, 85748 Garching via Munich, Germany*

<sup>4</sup>*Lund Observatory, Division of Astrophysics, Department of Physics, Lund University, Box 118, SE-221 00 Lund, Sweden*

<sup>5</sup>*Research School of Astronomy and Astrophysics, The Australian National University, Canberra, ACT 2611, Australia*

<sup>6</sup>*ACCESS-NRI, Australian National University, Canberra, ACT2601, Australia*

<sup>7</sup>*Observational Astrophysics, Department of Physics and Astronomy, Uppsala University, Box 516, 751 20 Uppsala, Sweden*

<sup>8</sup>*Lund Observatory, Department of Geology, Sölvegatan 12, 22362 Lund, Sweden*

<sup>9</sup>*Theoretical Astrophysics, Department of Physics and Astronomy, Uppsala University, Box 516, 751 20 Uppsala, Sweden*

<sup>10</sup>*School of Physics, University of New South Wales, Sydney, NSW 2052, Australia*

<sup>11</sup>*Faculty of Mathematics and Physics, University of Ljubljana, Jadranska 19, 1000 Ljubljana, Slovenia*

<sup>12</sup>*Sydney Institute for Astronomy, School of Physics, A28, The University of Sydney, Sydney, NSW 2006, Australia*

<sup>13</sup>*School of Physics and Astronomy, Monash University, Melbourne, VIC 3800, Australia*

<sup>14</sup>*Center for Computational Astrophysics, Flatiron Institute, 162 Fifth Avenue, New York, NY 10010, USA*

<sup>15</sup>*International Space Science Institute–Beijing, 1 Nanertiao, Zhongguancun, Hai Dian District, Beijing 100190, China*

Accepted 2026 May 29. Received 2026 May 27; in original form 2026 February 2

## ABSTRACT

We present a comprehensive data-driven spectroscopic analysis of 357,415 red giant stars using *Gaia* DR3 Radial Velocity Spectrometer (RVS) spectra (8460–8700 Å;  $R \approx 11, 500$ ), aimed at deriving precise stellar parameters and elemental abundances (collectively referred to as stellar labels). We employ *The Cannon*, a generative model based on 2747 giants in common with GALAH DR4, adopting GALAH labels ( $R \approx 28, 000$ ) for training. The resulting model predicts eleven stellar labels for RVS giants: effective temperature ( $T_{\text{eff}}$ ), surface gravity ( $\log g$ ), projected rotational velocity ( $v \sin i$ ), and abundances of [Fe/H], [Ca/Fe], [Si/Fe], [Ni/Fe], [Ti/Fe], as well as the neutron-capture elements [Zr/Fe], [Ce/Fe], and [Nd/Fe]. Building on these results, we develop a probabilistic framework to chemically identify debris from the *Gaia*–Sausage–Enceladus (GSE) accretion event. A logistic regression classifier, optimised via Markov Chain Monte Carlo sampling and trained on a small reference sample of GSE members and comparison stars, identifies stars with high GSE membership probabilities based solely on their chemical abundances, with the resulting candidates exhibiting distinctive abundance-ratio patterns, including [Ca/Ti], [Ti/Ce], and [Nd/Zr]. Applying independent kinematic constraints yields a robust sample of GSE candidates, demonstrating that the characteristic chemical signatures remain consistent after applying these constraints. This work demonstrates the power of data-driven analysis techniques to extract detailed chemical information from medium-resolution spectra and establishes a framework for tracing Galactic accretion events using chemical abundances.

**Key words:** stars: abundances – stars: fundamental parameters – techniques: spectroscopic – Galaxy: kinematics and dynamics – Galaxy: evolution – surveys

## 1 INTRODUCTION

Deciphering the formation and chemical evolution history of the Milky Way requires precise measurements of stellar parameters and elemental abundances across diverse Galactic populations. Large-scale spectroscopic surveys such as GALAH (GALactic Archaeology

\* E-mail: pradoshbarun.das@mq.edu.au, pbdrohan@gmail.com

† <https://www.galah-survey.org>

with HERMES; De Silva et al. 2015; Martell et al. 2017; Buder et al. 2018, 2021, 2025), APOGEE (Apache Point Observatory Galactic Evolution Experiment; Majewski et al. 2017), and *Gaia*-ESO (Gilmore et al. 2012; Randich et al. 2013) have provided transformative insights into the chemodynamical structure of the Galaxy. Complementing these, the ESA *Gaia* mission (Gaia Collaboration et al. 2016, 2018, 2023a) has yielded astrometric and photometric data for over a billion stars, with radial velocities and medium-resolution spectra from the Radial Velocity Spectrometer (RVS; Cropper et al. 2018; Recio-Blanco et al. 2016, 2023) for  $\sim 33$  million stars, enabling chemodynamical studies of the Milky Way (Gaia Collaboration et al. 2023b). However, the limited spectral resolution and relatively narrow wavelength range of *Gaia*-RVS ( $R \approx 11,500; 8460\text{--}8700 \text{ \AA}$ ) present significant challenges for detailed chemical abundance analyses using traditional methods, such as equivalent width measurements or spectral synthesis fitting, which require either higher spectral resolution or a wider wavelength baseline to resolve individual spectral features and constrain stellar parameters independently.

Data-driven approaches, on the other hand, can overcome these limitations to extract reliable stellar labels from lower-resolution spectra by exploiting the full stellar information encoded in each spectrum. One such method is *The Cannon* (Ness et al. 2015; Casey et al. 2016; Ho et al. 2017a), a generative model that uses a well-characterised training set to model the normalised spectral flux as a function of stellar labels, and infer those stellar labels for a much larger set. This approach has proven effective in combining the precision of high-resolution datasets with the scale of more extensive but noisier spectroscopic catalogues.

Since its initial application to APOGEE DR10 using a training sample of only 542 reference stars (Ness et al. 2015), *The Cannon* has been extensively validated across a wide range of spectroscopic surveys. Casey et al. (2016) extended *The Cannon* to detailed chemical abundance analyses with 17 stellar labels (including 15 elemental abundances) for 87,563 red giant stars. Ho et al. (2017a) applied *The Cannon* to transfer APOGEE labels ( $R \approx 22,500$ ) to 454,180 LAMOST giants ( $R \approx 1800$ ; Luo et al. 2015) using 9,952 common stars as training data, eliminating systematic label inconsistencies between surveys and producing the first  $[\alpha/M]$  measurements from LAMOST spectra. Ho et al. (2017b) used *The Cannon* to derive stellar masses and ages for 230,000 LAMOST giant stars from their carbon and nitrogen abundance signatures. Buder et al. (2018) applied *The Cannon* to 342,682 GALAH stars to measure 23 elemental abundances, demonstrating robust label transfer within a high-resolution optical spectroscopic survey. Wheeler et al. (2020) estimated abundances for nearly 3.9 million LAMOST stellar spectra across five nucleosynthetic channels using GALAH as reference data, whilst Nandakumar et al. (2022) employed *The Cannon* to construct a combined APOGEE–GALAH catalogue, demonstrating its utility to homogenise stellar labels across independent surveys. More recently, Das et al. (submitted) applied *The Cannon* to  $\sim 36,000$  *Gaia*-ESO survey HR15N spectra ( $R \approx 19,200; \lambda \approx 6440\text{--}6815 \text{ \AA}$ ) to derive Ba and Eu abundances, demonstrating the capability of the method to recover neutron-capture elemental abundances from intermediate-resolution spectra.

*The Cannon* is also well suited to *Gaia* DR3 RVS spectra, which, despite their lower spectral resolution, encompass key diagnostic features, including the near-infrared Ca II triplet and multiple absorption lines from  $\alpha$ -, Fe-peak, and neutron-capture elements. Das et al. (2025b) applied *The Cannon* to derive stellar parameters and elemental abundances for approximately 800,000 *Gaia*-RVS spectra using GALAH DR4 ( $R \approx 28,000$ ) as the reference set, trained on 14,484 stars in common between the two surveys. The resulting abundance

distributions, particularly the  $[\text{Ti/Fe}]$ – $[\text{Fe/H}]$  plane, clearly recovered the characteristic  $\alpha$ -element bimodality of Milky Way disc stars. Validation using open and globular cluster stars demonstrated metallicity precisions of approximately 0.02–0.10 dex, confirming that *The Cannon* can derive reliable stellar abundances from medium-resolution RVS spectra with high precision (see Fig. 10 in Das et al. 2025b). These results are consistent with independent analyses of the same dataset, such as Guiglion et al. (2024), who employed a Convolutional Neural Network (CNN) to derive stellar parameters, metallicities, and  $[\alpha/\text{Fe}]$  ratios from *Gaia* DR3 RVS spectra, also recovering the  $\alpha$ -bimodality of the Galactic disc.

In this work, we apply *The Cannon* to a curated sample of red giant stars with *Gaia* DR3 RVS spectra, using stellar parameters and elemental abundances from GALAH DR4 as the training labels. In particular, we extend the label space to include the neutron-capture elements Zr, Ce, and Nd – elements whose features are weak and often blended in medium-resolution spectra but which can provide valuable constraints on the chemical evolution of the Galaxy (Snedden et al. 2008; Recio-Blanco et al. 2023). These elements are common tracers of neutron-capture enrichment: Zr and Ce are dominated by the *s*-process at near-solar metallicities, while Nd receives significant contributions from both *s*- and *r*-processes (e.g. Sneden et al. 2008). Their abundance patterns are therefore especially useful for disentangling *in situ* versus accreted stellar populations and for constraining the timescales of chemical enrichment in different Galactic components. Our sample of 357,415 red giant stars drawn from the thin disk, thick disk, and halo enables a statistically robust investigation of Galactic chemical evolution and accreted stellar populations across diverse kinematic and chemical environments.

A key application of these chemical abundance labels is the identification of stars associated with the *Gaia*–Sausage–Enceladus (GSE) merger event (Belokurov et al. 2018; Helmi et al. 2018), one of the most significant accretion episodes in our Galaxy. This event deposited a population of stars with low angular momentum and highly eccentric orbits into the stellar halo. While previous GSE membership identification has relied primarily on kinematics, recent studies have emphasised the value of chemical abundance patterns for tracing accreted populations. Early work by Nissen & Schuster (2010) identified two chemically distinct halo populations in the solar neighbourhood via their  $[\text{Mg/Fe}]$ ,  $[\text{Na/Fe}]$  and  $[\text{Ni/Fe}]$  ratios. Subsequent work extended these diagnostics: Hawkins et al. (2015), Das et al. (2020), and Carrillo et al. (2022) used  $[\text{Al/Fe}]$  versus  $[\text{Mg/Mn}]$  to separate accreted stars, while Buder et al. (2022) demonstrated the utility of  $[\text{Na/Fe}]$  versus  $[\text{Mg/Mn}]$  in identifying GSE members. However, in this study we do not have measurements for all of these key elements. Instead, to identify new potential GSE candidates, we build a probabilistic classification model based solely on available chemical abundances. Using logistic regression optimised via Markov Chain Monte Carlo (MCMC), we infer GSE membership probabilities for our full sample. This is followed by a kinematic refinement based on orbital parameters derived from Galactocentric velocities and integrals of motion. By incorporating additional elemental abundances and a larger sample of stars, our study aims to better characterise the complex spatial, chemical, and dynamical structure of GSE, potentially reconciling differences in the metallicity distributions reported in previous studies (see, e.g., Fig. 10 in Buder et al. 2022).

The structure of this paper is as follows: Section 2 describes the dataset used in our *The Cannon* model, including the *Gaia* DR3 RVS spectra and GALAH DR4 labels. A description of *The Cannon*’s algorithm, including an overview of various selection criteria for the training sample as well as the flagging procedures of the red giant stars in the sample, is provided in Section 3. In Section 4,

we assess the significance of the *The Cannon*-predicted elemental abundances of neutron-capture elements in RVS spectra using differential analysis and cross-correlation techniques. Then, using the final *The Cannon* catalogue of stellar abundances, Section 5 discusses the empirical probabilistic model developed using MCMC methods to chemically identify GSE candidates based solely on elemental abundances, followed by a dynamical analysis to refine the GSE candidate sample. Finally, Section 6 summarises our findings and implications for upcoming spectroscopic datasets such as *Gaia* DR4.

## 2 DATA

The primary data set utilised in this study is the catalogue<sup>1</sup> from Das et al. (2025b), which provides *The Cannon* predictions for eight stellar labels – three stellar parameters and five elemental abundances – for a total of 796,633 *Gaia*-RVS stars. We applied the `flag_cannon = 0` quality criteria to ensure reliable stellar parameters, and used the  $\log g$  values from Das et al. (2025b) to select our initial sample of 357,415 giant stars ( $\log g < 3.5$  dex). In our analysis, we use the corresponding stellar spectra from *Gaia* DR3 RVS<sup>2</sup> and incorporate stellar parameters ( $T_{\text{eff}}$ ,  $\log g$ ,  $v \sin i$ ) along with chemical abundances ([Fe/H], [Ca/Fe], [Si/Fe], [Ni/Fe], [Ti/Fe], [Ce/Fe], [Zr/Fe], and [Nd/Fe]) from GALAH DR4 (Buder et al. 2025) to train the model using *The Cannon*.

### 2.1 Gaia-RVS

The *Gaia* Radial Velocity Spectrometer (RVS) is a near-infrared spectrograph (Cropper et al. 2018; Gaia Collaboration et al. 2018, 2023a) on the ESA *Gaia* satellite, designed to obtain radial velocities, spectral classifications, and astrophysical parameters for bright stars as part of *Gaia*'s astrometric and photometric survey mission. Spanning 8460–8700 Å at a resolving power of  $R \approx 11,500$ , RVS targets the Ca II triplet region, suitable for determining stellar kinematics and metallicities across a wide range of spectral types.

RVS spectra are acquired for stars brighter than  $G \sim 16$  mag, with radial velocities for progressively fainter and more complex targets to be published in successive data releases. *Gaia* DR3 provides radial velocities for over 33 million stars (Recio-Blanco et al. 2023), along with median RVS spectra for  $\sim 1$  million bright sources. These spectra are corrected for background and instrumental effects and co-added from multiple *Gaia* transits.

In addition to radial velocities, the RVS spectra also yield stellar atmospheric parameters and chemical abundances through the *Gaia* astrophysical parameter inference pipeline, GSP-Spec (Recio-Blanco et al. 2016, 2023). For bright stars ( $G \lesssim 12$  mag), *Gaia* DR3 provides estimates of quantities such as  $T_{\text{eff}}$ ,  $\log g$ , [M/H], and abundances for a limited number of elements based on comparisons with synthetic spectral grids (Recio-Blanco et al. 2023). The combination of RVS data with *Gaia* astrometry and photometry enables full six-dimensional phase-space mapping and chemodynamical studies of the Galaxy, particularly in the Solar neighbourhood.

### 2.2 GALAH Data Release 4

The GALAH survey is a high-resolution spectroscopic initiative conducted using the HERMES spectrograph (Brzeski et al. 2011; Heij-

mans et al. 2012; Sheinin et al. 2015) on the 3.9-m Anglo-Australian Telescope, operating at  $R \approx 28,000$ . HERMES collects spectra in four discrete optical channels – 4713–4903 Å (blue), 5648–5873 Å (green), 6478–6737 Å (red), and 7585–7887 Å (near-infrared) – optimised for elemental abundance analysis. The instrument is fibre-fed by the 2-degree Field (2dF) positioner (Lewis et al. 2002), allowing simultaneous observation of up to 392 stars over a 2-degree field of view. GALAH comprises two observational phases with complementary targeting strategies (Buder et al. 2025): Phase-1 (DR1–DR3) targets nearby stars predominantly within  $\sim 4$  kpc of the Sun whilst avoiding the Galactic plane ( $|b| > 10^\circ$ ), whereas Phase-2 (incorporated into DR4) explicitly targets the Galactic plane at low Galactic latitudes to constrain the structure and chemical signatures of inner-disk and bulge populations. GALAH DR4 additionally includes dedicated observations of more than 300 stellar clusters, providing a diverse sample spanning from the local solar neighbourhood to the inner Galaxy.

We use GALAH DR4 (Buder et al. 2025), which provides spectra for 917,588 stars. It incorporates data from GALAH Phases 1 and 2, TESS-HERMES (Sharma et al. 2018), K2-HERMES (Sharma et al. 2019), and observations of open and globular clusters. The catalogue includes abundances for up to 32 elements for these stars. For this study, we select a subset of GALAH DR4 stars that meet quality control criteria: `flag_sp = 0` (valid spectral synthesis solution with no spectral peculiarities), `flag_fe_h = 0` and `flag_x_fe = 0`, where  $x$  refers to each chemical element of interest. This ensures robust stellar labels for training and inference.

## 3 METHOD

### 3.1 The Cannon

*The Cannon* (Ness et al. 2015; Ho et al. 2017a) is a probabilistic, data-driven generative model designed to estimate stellar atmospheric parameters and elemental abundances by modelling normalised stellar spectra as a function of stellar labels. It relies on a reference set of spectra for which high-fidelity labels are known. Using these, it trains a forward model that predicts the flux at each pixel as a smooth function of the stellar labels. In its original formulation, the model is trained by optimising the likelihood of the observed flux at each wavelength pixel, assuming that the flux at wavelength  $\lambda$  for star  $n$  can be expressed as:

$$G_{n\lambda} = f(l_n) \cdot \theta_\lambda + \epsilon_{n\lambda}. \quad (1)$$

Here,  $f(l_n)$  is a vectorising function of the stellar labels  $l_n$  (typically a quadratic polynomial),  $\theta_\lambda$  is the coefficient vector at pixel  $\lambda$ , and  $\epsilon_{n\lambda}$  is the residual. During training,  $\theta_\lambda$  and an additional intrinsic scatter term  $s_\lambda$  are optimised to maximise the total log-likelihood across the training set (Ness et al. 2015; Casey et al. 2016). The residual  $\epsilon_{n\lambda}$  accounts for both the observational uncertainty  $\sigma_{n\lambda}$ , which represents the per-pixel flux error, and the intrinsic model scatter  $s_\lambda$ , which captures astrophysical variance not explained by the model. These contributions combine in quadrature to give the total variance:

$$\sigma_{\text{tot},n\lambda}^2 = \sigma_{n\lambda}^2 + s_\lambda^2. \quad (2)$$

Under the Gaussian noise assumption, the residual  $\epsilon_{n\lambda}$  is therefore distributed as:

$$\epsilon_{n\lambda} \sim \mathcal{N}(0, \sigma_{\text{tot},n\lambda}^2). \quad (3)$$

In other words, the observed residuals reflect both measurement noise and intrinsic scatter in the model. The training procedure involves

<sup>1</sup> <https://cdsarc.cds.unistra.fr/viz-bin/cat/JMNRAS/538/605>

<sup>2</sup> <https://doi.org/10.17876/gaia/dr.3/54>

maximising the following log-likelihood for each wavelength independently:

$$\ln p(G_{n\lambda}|\theta_\lambda, f(l_n), s_\lambda^2) = -\frac{[G_{n\lambda} - f(l_n) \cdot \theta_\lambda]^2}{2(\sigma_{n\lambda}^2 + s_\lambda^2)} - \frac{1}{2} \ln(\sigma_{n\lambda}^2 + s_\lambda^2). \quad (4)$$

Once trained, the coefficients  $\theta_\lambda$  and  $s_\lambda$  are fixed. For an unlabelled test spectrum, stellar labels are inferred by maximising the likelihood of the observed flux with respect to the labels:

$$l_m \leftarrow \arg \min_l \sum_{\lambda=1}^{N_\lambda} \frac{[G_{m\lambda} - f(l) \cdot \theta_\lambda]^2}{\sigma_{m\lambda}^2 + s_\lambda^2}. \quad (5)$$

This formulation allows *The Cannon* to robustly transfer label information from higher signal-to-noise ratio (SNR) training data to lower SNR test spectra without requiring the training and test sets to be statistically identical. Moreover, its fully generative design makes it amenable to cross-calibration across heterogeneous spectroscopic surveys (e.g., APOGEE, LAMOST, GALAH, *Gaia*-DR3 RVS), as demonstrated in applications such as [Ho et al. \(2017a\)](#), [Buder et al. \(2018\)](#), [Wheeler et al. \(2020\)](#), [Nandakumar et al. \(2022\)](#), and [Das et al. \(2025b\)](#). In this work, we adopt the framework of *The Cannon*<sup>3</sup> ([Ness et al. 2015](#); [Casey et al. 2016](#)), constructing a second-order polynomial model in label space and training it on a selected reference set. This enables us to propagate labels to our target sample while maintaining physical interpretability throughout the sample.

### 3.2 Training Data Set

From the total sample of 357,415 giant stars ( $\log g < 3.5$  dex, see Sec. 2) selected from the catalogue ([Das et al. 2025a](#)), we further refined the selection conditions to create a training sample focused on extracting more localised chemical information and individual elemental abundances. The training data set was generated by adhering to the quality criteria explained below and additional [Fe/H] quality cuts for the training sample.

To ensure a representative training sample, including stars over a broad metallicity range, a comparable number of stars were selected in different metallicity bins using multiple criteria. Stars from the *Gaia*-RVS dataset with GALAH metallicity labels of  $[\text{Fe}/\text{H}] < -0.8$  dex were required to have a *Gaia*-RVS spectral SNR  $\geq 25$  and GALAH spectral SNR ( $\text{snr\_px\_ccd3}$ )  $\geq 30$ . Additional selection criteria included GALAH effective temperature,  $T_{\text{eff}} < 7000$  K, *Gaia* renormalised unit weight errors ( $\text{ruwe}$ )  $< 1.2$ , GALAH chi-squared values ( $\text{chi2\_sp}$ )  $< 4$ , positive *Gaia* parallaxes ( $\text{parallax}$ )  $> 0$  mas, and satisfying flags from the GALAH data reduction process, which ensured reliability of both the spectral data and the derived elemental abundances. In addition to this, we also included stars with GALAH metallicity labels for  $[\text{Fe}/\text{H}] > -0.8$  dex with more stringent criteria in addition to the above-mentioned conditions: *Gaia*-RVS SNR  $\geq 50$ , GALAH SNR  $\geq 50$  across all four CCD arms, and small uncertainties associated with GALAH DR4 chemical abundances ( $\leq 0.10$  dex) and stellar parameters ( $e_{T_{\text{eff}}} \leq 80$  K, and  $e_{\log g} \leq 0.10$  dex) to ensure data quality and reliability. Following these cuts, the new training sample comprised 2747 stars, which were categorised into three metallicity ranges: 833 stars with  $-2.0 < [\text{Fe}/\text{H}]$  (dex)  $\leq -0.8$ , 1165 stars with  $-0.8 < [\text{Fe}/\text{H}]$  (dex)  $\leq 0$ , and 749 stars with  $[\text{Fe}/\text{H}] > 0$  dex. Such distribution of stars in the metallicity space provides

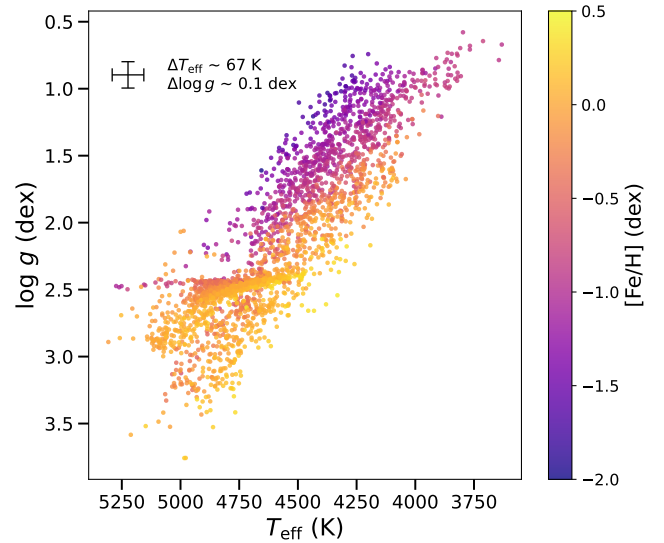


**Figure 1.** Kiel Diagram showing the GALAH values for  $\log g$  versus  $T_{\text{eff}}$ , colour coded with  $[\text{Fe}/\text{H}]$  for the 2747 stars selected in the training sample. The representative error bar in the lower-right corner indicates the median uncertainties ( $\Delta T_{\text{eff}} \sim 67$  K and  $\Delta \log g \sim 0.1$  dex) estimated in GALAH for the training sample.

a comprehensive coverage that is essential for robust predictions in subsequent test samples (see Fig. 1).

For the analysis using *The Cannon*, a total of eleven stellar labels from GALAH DR4 were employed, including the stellar parameters ( $T_{\text{eff}}$ ,  $\log g$ ,  $v \sin i$ ) and elemental abundances ( $[\text{Fe}/\text{H}]$ ,  $[\text{Ca}/\text{Fe}]$ ,  $[\text{Si}/\text{Fe}]$ ,  $[\text{Ni}/\text{Fe}]$ , and  $[\text{Ti}/\text{Fe}]$ ), as well as the neutron-capture elements ( $[\text{Zr}/\text{Fe}]$ ,  $[\text{Ce}/\text{Fe}]$ , and  $[\text{Nd}/\text{Fe}]$ ). The trained model was then applied to predict these 11 stellar labels for the full sample of 357,415 giant stars ( $\log g < 3.5$  dex). The choice of these elements was motivated by [Recio-Blanco et al. \(2023\)](#), who analysed these species within the *Gaia*-RVS wavelength range; we adopted the same set of elements following previous studies in this spectral region. Some elements present in the *Gaia*-RVS wavelength range were not included as training labels; Sulphur is not available in GALAH DR4, CN suffers from degeneracies between carbon and nitrogen abundances that prevent reliable measurements, and the Cr, Mg, Co and O lines in the RVS range are generally weak and provide limited diagnostic information.

Although the neutron-capture elements Zr, Ce, and Nd also exhibit weak lines, this study extends the application of *The Cannon* to the recovery of their abundances and evaluates its performance on medium-resolution, relatively low-SNR RVS spectra. To ensure that the stellar label space spanned by the training sample is representative of the test stars, we performed a 12-fold cross-validation using *The Cannon* to evaluate its performance in predicting stellar parameters and elemental abundances. For this analysis, the dataset of 2747 stars was randomly divided into 12 subsets. In each iteration of the cross-validation, one subset was withheld as a validation set, while the model was trained on the remaining 11 subsets. The trained model was then employed to predict the stellar labels of the withheld subset. This methodology allowed us to calculate the Root-Mean-Square Error (RMSE) and biases, defined as the differences between the mean values predicted by *The Cannon* and the reference values from GALAH DR4, for the model trained on this dataset. The RMSE and bias metrics for the stellar parameters derived from the training sample are presented in Table 1. These cross-validation statistics

<sup>3</sup> <https://github.com/andycasey/AnniesLasso>

**Table 1.** Biases and RMSE values of the 12-fold cross-validation test for the *Gaia*-RVS training sample consisting of 2747 giants ( $\log g < 3.5$  dex) trained by *The Cannon* using stellar parameters and abundances from GALAH DR4 survey.

Stellar Label	RMSE	Bias
$T_{\text{eff}}$ (K)	70	12
$\log g$ (dex)	0.14	0.01
$v \sin i$ (km s $^{-1}$ )	1.93	0.18
[Fe/H] (dex)	0.09	0.01
[Ca/Fe] (dex)	0.08	0.00
[Si/Fe] (dex)	0.06	0.01
[Ni/Fe] (dex)	0.04	0.00
[Ti/Fe] (dex)	0.05	0.00
[Zr/Fe] (dex)	0.15	0.02
[Ce/Fe] (dex)	0.18	0.02
[Nd/Fe] (dex)	0.15	0.01

provide an estimate of the internal precision of the model within the training set.

Fig. 2 shows the one-to-one comparisons between the stellar labels predicted by *The Cannon* and the corresponding GALAH DR4 reference labels, while Fig. 3 presents the distributions of the residuals relative to the GALAH values. Overall, the predicted stellar labels exhibit good agreement with the reference labels, with small residual dispersions, demonstrating that the model is able to reproduce the GALAH DR4 labels with high precision. Although *The Cannon* provides robust label estimates across the full sample, predictions may be less reliable for spectra located near the boundaries of the training-label space or for lower signal-to-noise ratio observations, where the associated uncertainties are correspondingly larger.

### 3.3 Application of *The Cannon* on *Gaia*-RVS spectra

Using the model developed with the training set, we applied *The Cannon* to predict stellar labels for the sample of 357,415 *Gaia*-RVS targets. The model was supplied with spectral fluxes (`f_lux`) and their associated flux errors (`err_flux`) for these *Gaia*-RVS targets, which allowed us to predict the stellar labels, including  $T_{\text{eff}}$ ,  $\log g$ ,  $v \sin i$ , [Fe/H], [Ca/Fe], [Si/Fe], [Ni/Fe], [Ti/Fe], [Zr/Fe], [Ce/Fe], and [Nd/Fe] (hereafter, the labels). To ensure the validity of the model’s predictions, it is essential to flag *The Cannon*’s estimates that lie outside the parameter range covered by the training set. This is essential for the accuracy of the predictions, which may decrease when extrapolating to regions outside the bounds of the training data. For each test star  $n$  and each training star  $j$ , we define a normalised squared distance in label space (Ho et al. 2017a; Buder et al. 2018; Nandakumar et al. 2022; Das et al. 2025b),

$$d_{nj}^2 = \sum_l \frac{(l_{n,l}^{\text{Cannon}} - l_{j,l}^{\text{GALAH}})^2}{K_l^2}, \quad (6)$$

where the sum runs over all labels  $l$  in the model,  $l_{n,l}^{\text{Cannon}}$  is *The Cannon*’s prediction for label  $l$  of test star  $n$ ,  $l_{j,l}^{\text{GALAH}}$  is the corresponding GALAH DR4 label for training star  $j$ , and  $K_l$  is a characteristic scale for label  $l$ . We adopt  $K_l$  equal to the RMSE values obtained for the labels from the 12-fold cross-validation of the training sample (Table 1), which provide an empirical measure of the typical label scatter in the training set.

For each test star  $n$ , we identify the set  $\mathcal{N}_n$  of the  $N_{\text{nn}} = 10$  training stars with the smallest  $d_{nj}$  values (i.e. the ten nearest neighbours in label space). We then define the average nearest-neighbour distance:

$$D_n = \frac{1}{N_{\text{nn}}} \sum_{j \in \mathcal{N}_n} d_{nj}. \quad (7)$$

Small values of  $D_n$  indicate that the test star lies within a well-sampled region of the training-set label space, while large values indicate potential extrapolation. Following Das et al. (2025b), we adopt a global threshold  $D_n < 2\sigma$  for all the labels together to define stars that are sufficiently close to the training-set manifold in this normalised label space. Stars satisfying  $D_n < 2\sigma$  for all the labels are assigned `flag_cannon` = 0, while those with  $D_n \geq 2\sigma$  are assigned `flag_cannon` = 1. Out of the 357,415 *Gaia*-RVS targets, 314,010 stars meet the  $D_n < 2\sigma$  criterion and are considered to have labels within the limits of the total label space spanned by the training set.

In addition to the global `flag_cannon`, we also define element-specific flags to assess the reliability of individual abundance measurements. For each element  $X \in \{\text{Ca, Ti, Si, Ni, Nd, Ce, Zr}\}$ , we compute a corresponding nearest-neighbour distance in a reduced label space, including only the stellar parameters ( $T_{\text{eff}}$ ,  $\log g$ ,  $v \sin i$ ), [Fe/H] and the abundance  $[X/\text{Fe}]$ . Using the same normalisation scheme as in Eq. 7, we define an element-wise distance  $D_n^{(X)}$ . We then adopt a similar threshold criterion, such that stars with  $D_n^{(X)} < 2\sigma$  are considered to lie within the well-sampled region of the training-set manifold for that specific element and are assigned `flag_XFe` = 0. Conversely, stars with  $D_n^{(X)} \geq 2\sigma$  are flagged as `flag_XFe` = 1, indicating that the corresponding abundance may be affected by extrapolation beyond the training-set coverage.

We also note that the internal scatter terms  $s_{\text{I}}$  introduced by *The Cannon* (Section 3.1) describe intrinsic model scatter in flux space and do not by themselves account for the full, SNR-dependent uncertainty of the inferred stellar labels. In addition to these internal contributions, there are external effects arising from finite SNR and other observational systematics, which can be parameterised as a function of spectral SNR (e.g. Ness et al. 2015; Wheeler et al. 2020; Manea et al. 2024). Following a similar approach to Das et al. (2025b), we therefore generate  $N_{\text{rep}} = 10$  independent noise realisations of each *Gaia*-RVS spectrum in our test sample of 357,415 stars. For each realisation, the flux at every wavelength pixel is redrawn from a normal distribution with mean equal to the observed flux and standard deviation equal to the reported per-pixel uncertainty. This procedure produces 10 synthetic spectra per star that incorporate SNR-dependent flux variations consistent with the observational noise. We apply *The Cannon* to each of these 10 noise realisations, obtaining 10 independent estimates of each of the 11 stellar labels for every star. For a given star  $n$  and label  $l$ , we define the observational, SNR-dependent label uncertainty as the standard deviation of these noise-based estimates,

$$\sigma_{n,l}^{\text{obs}} = \text{StdDev}\left(l_{n,l}^{(1)}, l_{n,l}^{(2)}, \dots, l_{n,l}^{(N_{\text{rep}})}\right), \quad (8)$$

where  $l_{n,l}^{(k)}$  denotes the value of label  $l$  for star  $n$  in the  $k$ -th realisation. In addition, *The Cannon* provides an internal covariance matrix in label space for each star, which reflects the curvature of the likelihood around the best-fitting solution. We characterise the corresponding internal uncertainty for label  $l$  by the square root of the relevant diagonal element of this covariance matrix, denoted by  $\sigma_{n,l}^{\text{int}}$ . The total variance in label  $l$  for star  $n$  is then obtained by adding the observational and internal contributions in quadrature,

$$\sigma_{n,l,\text{tot}}^2 = \left(\sigma_{n,l}^{\text{obs}}\right)^2 + \left(\sigma_{n,l}^{\text{int}}\right)^2 \quad (9)$$

The uncertainty reported in our catalogue for each star and label

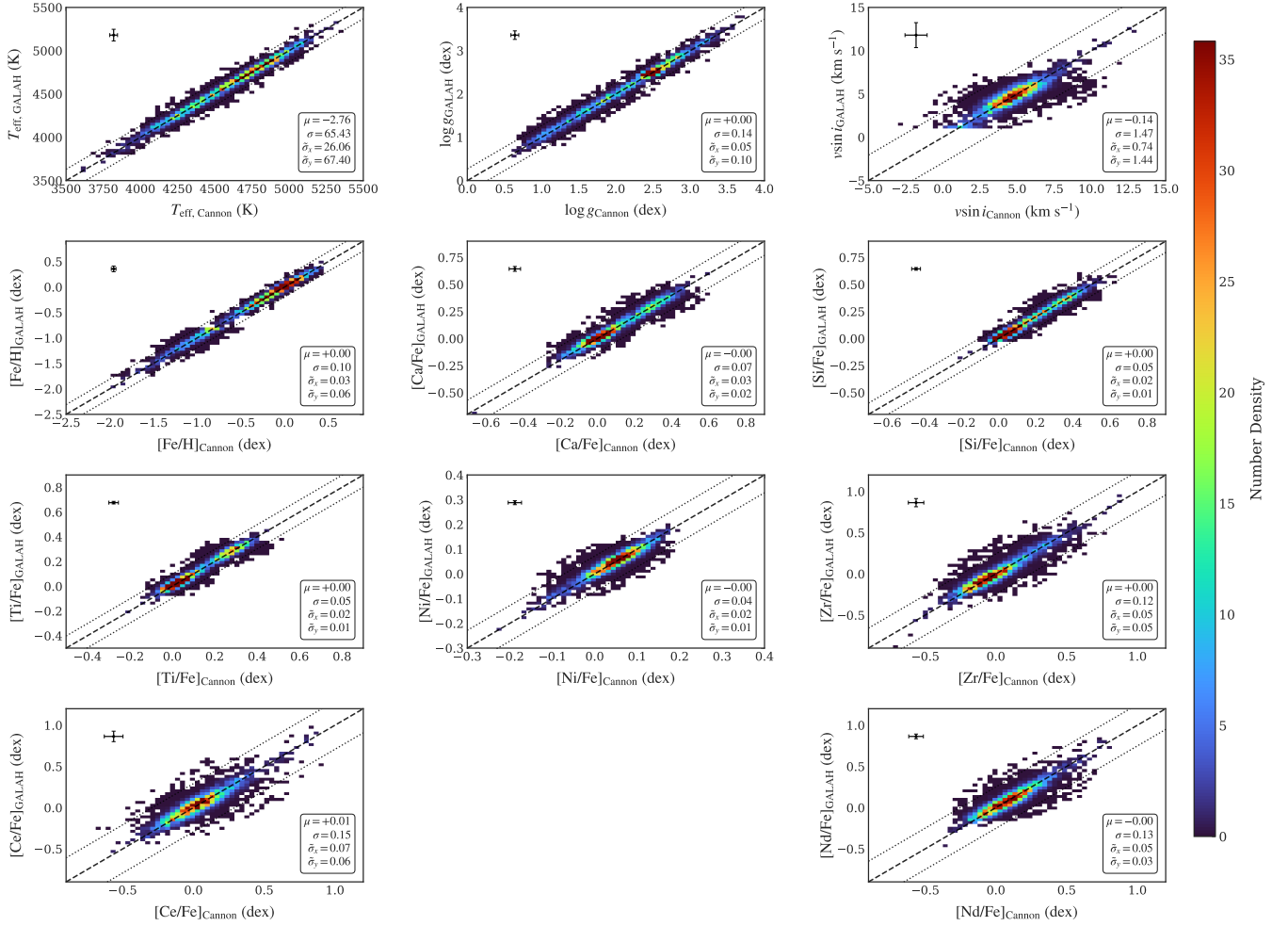


**Figure 2.** One-to-one relations for *The Cannon*-predicted stellar labels for the 2747 *Gaia*-RVS spectra of giants in the training sample. The horizontal axis indicates *The Cannon* predictions of the stellar parameters and abundances, and the vertical axis shows the literature values from GALAH DR4. The black dashed line indicates the one-to-one relation, while the dotted lines mark  $\pm 2\sigma$ , where  $\sigma$  is the standard deviation of the residuals (*The Cannon* predictions – GALAH DR4). The representative error bar in the upper-left corner of each panel denotes the median uncertainties in the *The Cannon* predictions and the GALAH DR4 labels.  $\mu$  and  $\sigma$  indicate the mean and standard deviation of the residuals, respectively, while  $\hat{\sigma}_x$  and  $\hat{\sigma}_y$  represent the median uncertainties in the *The Cannon* and GALAH DR4 labels.

is the square root of this total variance ( $\sqrt{\sigma_{n,l,tot}^2}$ ), which allows us to assess the reliability of the individual label measurements (see Table A1). We also compute reduced- $\chi^2$  values ( $r\_chi\_sq$ ) to assess the goodness-of-fit between *The Cannon*-predicted spectra and observed RVS spectra for each star (see Fig. A1). The  $r\_chi\_sq$  distribution peaks at  $\approx 1$  for the majority of stars, demonstrating reliable spectral reconstruction by *The Cannon*.

The performance of the model across the full signal-to-noise range is assessed by examining the inferred abundance uncertainties as a function of spectral SNR for all stellar labels (see Fig. C1). We find a continuous increase in uncertainties toward lower SNR, consistent with the expected decrease in spectral information content. We do not observe any abrupt degradation at low SNR, suggesting that the model remains stable in this regime. This provides a quantitative estimate of the achievable precision as a function of SNR for all the stellar labels. This trend also offers a complementary guideline for using the catalogue. By relating the reported uncertainties to spectral SNR, the results provide an empirical basis for selecting SNR thresholds corresponding to a desired level of precision. Depending on the scientific application, more stringent SNR or uncertainty cuts may

be adopted to construct high-precision samples, or more inclusive selections for statistical studies. The label uncertainty–SNR relation presented in Appendix C is intended to facilitate such choices.

#### 4 ASSESSING NEUTRON-CAPTURE ABUNDANCES WITH *The Cannon*

The atomic transition lines of neutron capture elements like Ce, Zr, and Nd are typically quite weak compared to other absorption features at these wavelengths, such as other atomic transitions or molecular absorption. This difference in line strengths becomes a challenge when determining chemical abundances from medium-resolution data at low or moderate SNR. A common solution to this issue is to fit a synthetic spectrum or equivalent widths (EW) to the observed spectrum to determine its chemical composition. However, applying these methods to a large dataset like ours is unfeasible due to the weaknesses of the lines, and the computational resources required by these approaches. Data-driven methods such as *The Cannon* can address this issue by learning from a well-studied reference set of

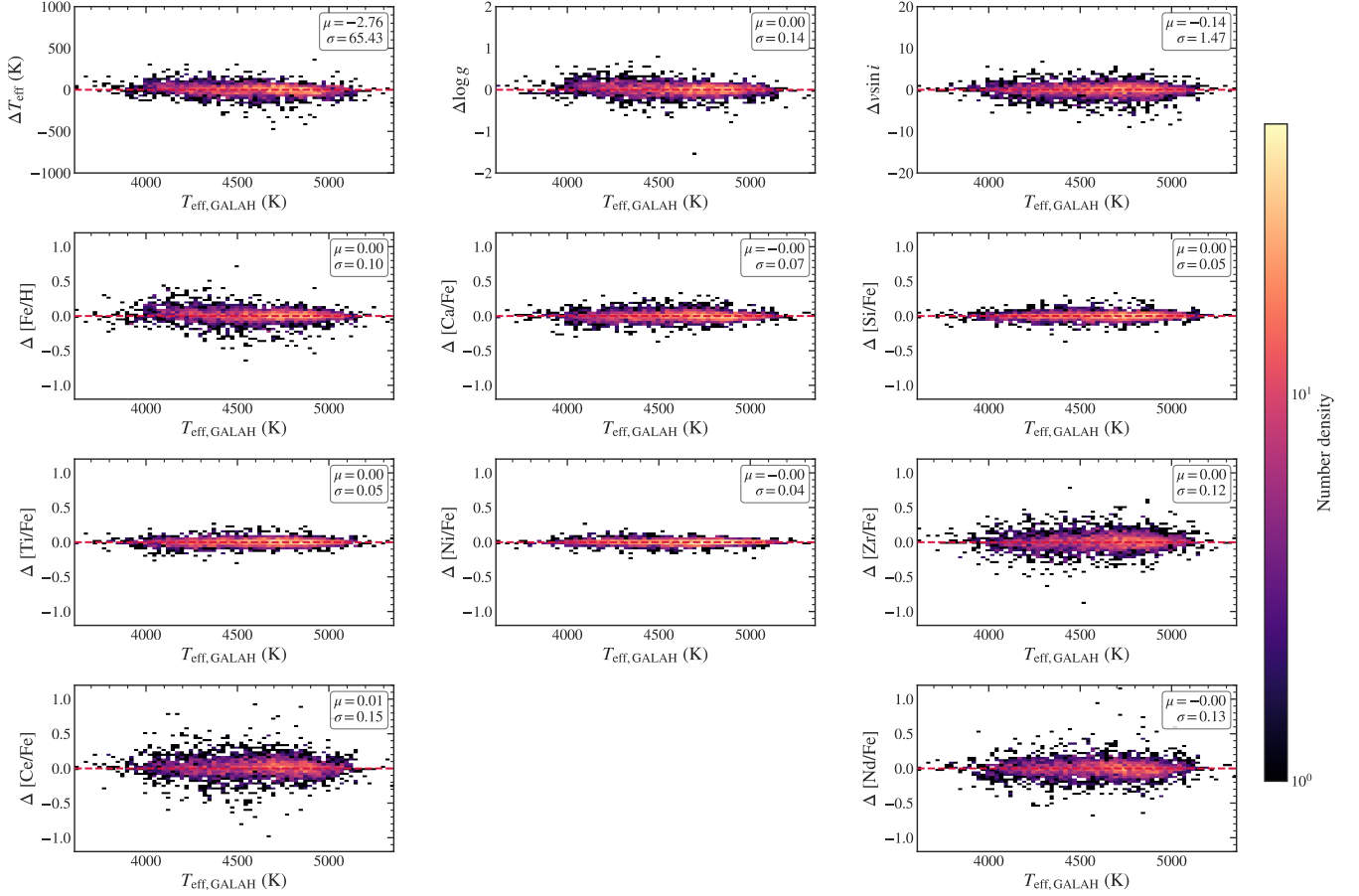


**Figure 3.** Residual values for *The Cannon*-predicted stellar labels (see Fig. 2). The horizontal axis shows  $T_{\text{eff}}$  values from GALAH DR4, and the vertical axis represents the difference between *The Cannon* predictions and GALAH DR4 values (*The Cannon* - GALAH DR4) for each of the stellar labels.  $\mu$  and  $\sigma$  represent the mean and standard deviation of the residual values respectively.

spectra – the training sample – for which a model is constructed using labels from another, typically higher resolution dataset (in this case, GALAH DR4).

Given that this method does not explicitly measure the strengths of identified absorption features – or the many other steps entailed by more traditional analysis techniques – a key question arises: can *The Cannon* reliably recover chemical abundances from weak absorption lines, or could its outputs simply reflect trends in Galactic chemical evolution learned from the training sample? Specifically, in this case, can *The Cannon* actually measure the abundances of individual neutron-capture elements, or is it in fact simply tracing some composite of neutron-capture features, or even other elements whose abundances track with the neutron-capture elements? To address these questions, we inspected the *Gaia*-RVS spectral regions corresponding to these elements and evaluated the significance of the absorption features of interest.

#### 4.1 Differential analysis of neutron-capture element absorption features

Within the *Gaia*-RVS wavelength range, Ce, Zr, and Nd have 8, 11, and 11 lines, respectively. The parameters of these n-capture lines are shown in Table D1. Note that for the species, we follow standard nomenclature to refer to the neutral states as X.0 and the ionised states as X.1, where X is the Z-number of the element.

Fig. 4 shows the observed spectrum from *Gaia*-RVS for a star in our sample with higher predicted Nd content from *The Cannon*,  $[\text{Nd}/\text{Fe}] = 0.61$  dex (Gaia ID: 680901874478777024, shown in blue). We compare this star with another of similar stellar parameters ( $T_{\text{eff}}/\log g/[\text{Fe}/\text{H}]$ ) but with a predicted Nd abundance of  $[\text{Nd}/\text{Fe}] = -0.02$  dex (Gaia ID: 51670728611455360, in red). The flux errors reported by *Gaia*-RVS for these two stars are represented with shaded regions in their respective colours. In this figure, the top two panels display the locations of the Nd lines along the spectra, marked with dashed vertical lines and yellow shading for both stars (A, B, C, D...), followed below by the residuals of their difference. The bottom set of panels provides a closer look at these Nd lines and their residuals, with the line centre wavelengths indicated in the middle of each panel, again marked by a dashed vertical line and a yellow-shaded region.

This *pseudo*-differential analysis (for a more rigorous application of differential analysis of chemical abundances, see, e.g., McKenzie et al. 2022; Monty et al. 2023) illustrates the flux differences between the two stars at  $\Delta[\text{Nd}/\text{Fe}] \sim 0.60$  dex. While small – on the level of at most a few percent – these star to star flux differences at the line locations show that there is information for *The Cannon* to work with, even at the moderate resolution of *Gaia*-RVS.

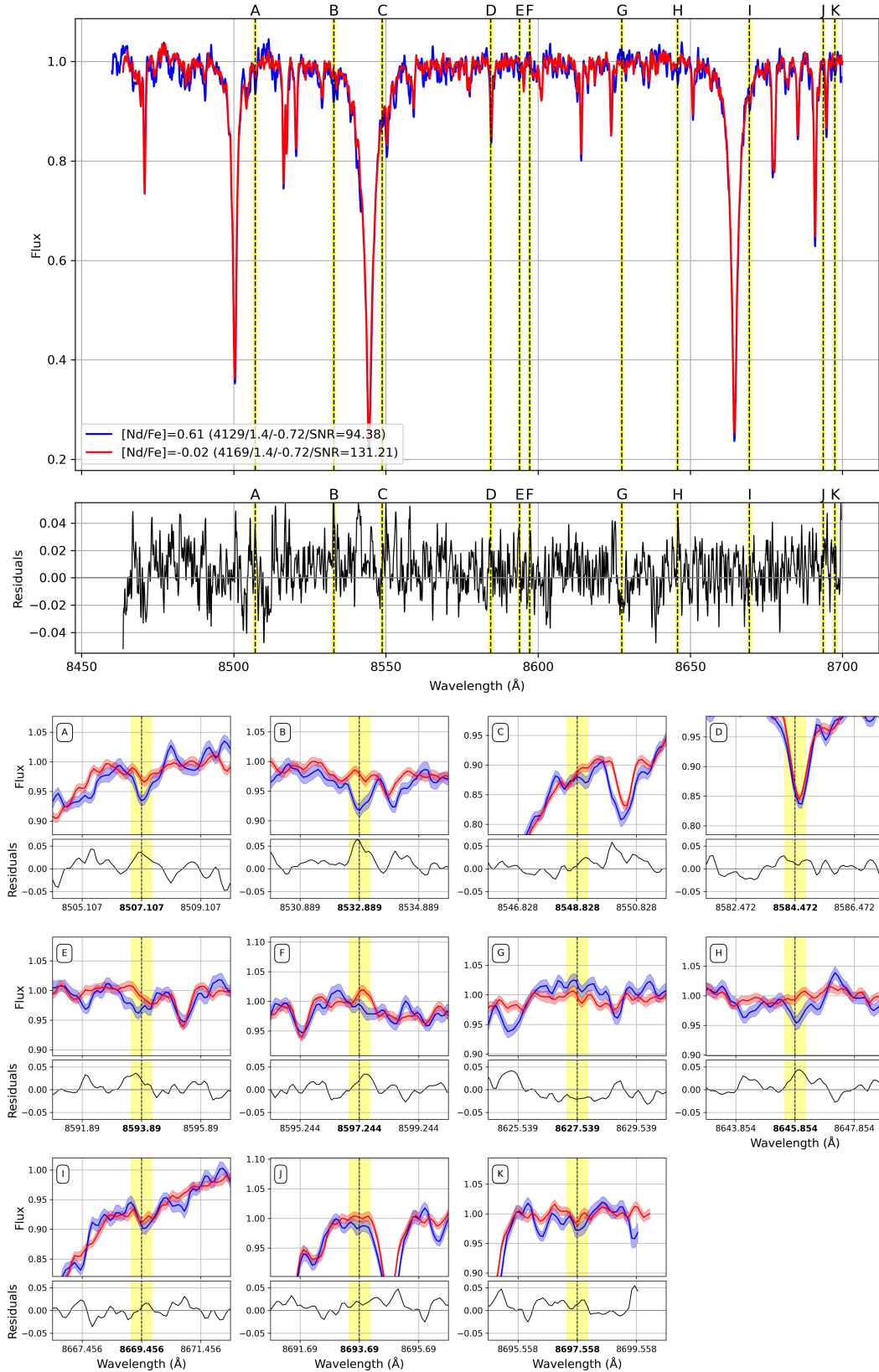


**Figure 4.** Comparison of two stars in our sample with similar stellar parameters and  $\Delta[\text{Nd}/\text{Fe}] \sim 0.60$  dex. The *Gaia*-RVS spectra correspond to a star with a higher Nd abundance predicted by *The Cannon*,  $[\text{Nd}/\text{Fe}] = 0.61$  dex (blue; Gaia ID: 680901874478777024) and another with  $[\text{Nd}/\text{Fe}] = -0.02$  dex (red; Gaia ID: 51670728611455360). The Nd abundances and stellar parameters and SNR ( $T_{\text{eff}}/\log g/[\text{Fe}/\text{H}]/\text{SNR}$ ) of both stars are shown at the bottom left of the top-main panel. Shaded regions indicate flux uncertainties as reported by *Gaia*-RVS. The location of the Nd absorption features are marked by dashed vertical lines and yellow shading (A, B, C, D . . .). The middle panel shows flux residuals, while the bottom set of panels provide a zoom-in view of the Nd lines and their residuals with their line-centre wavelengths highlighted at the bottom.

## 4.2 Verifying the presence of neutron-capture element lines through cross-correlation

In certain cases, such as with ionised Calcium (Ca II), we can visually confirm the absorption lines, providing a clear verification of the model’s accuracy. Additionally, cross-checking the abundance values with the GALAH DR4 test set further demonstrates that our model is a reasonable fit to the data. However, visually confirming the absorption lines for neutron-capture elements present in the *Gaia*-RVS spectra (such as Zr, Ce, and Nd) is challenging given the weakness of the lines (see, e.g., Fig. 4) and the low SNR of the *Gaia*-RVS spectra.

To address this issue, we use the cross-correlation technique (Snellen et al. 2010). This method has previously been used to detect species in the noise-dominated absorption and emission spectra of exoplanet atmospheres. In our case, we apply this technique to visually confirm the presence of neutron-capture elements within the *Gaia*-RVS wavelength span by taking a weighted average of all lines predicted to be present within the spectrograph’s wavelength range:

$$c(v) = \sum_{i=0}^N x_i \hat{T}_i(v) \quad (10)$$

Here,  $x_i$  refers to each spectral pixel,  $\hat{T}_i(v)$  are the sets of statistical weights used to compute the average, and  $v$  is the Doppler velocity. This equation calculates  $c(v)$ , the cross-correlation function that represents the weighted average of spectral lines as a function of Doppler velocities. In the case of an exoplanet transit, Doppler shift is necessary as the planet’s signal shifts throughout the observation. For stars, the signal will be located at an approximate Doppler shift of  $0 \text{ km s}^{-1}$ , as each RVS spectrum is shifted to the stellar rest frame. The set of statistical weights  $\hat{T}_i(v)$  is obtained by computing the expected line positions and depths for a particular star in the data set, Gaia ID: 6082274849118517248. For this star, we produce synthetic spectra using the local thermodynamic equilibrium (LTE) stellar line analysis program MOOG<sup>4</sup> (Snedden 1973) coupled with one-dimensional LTE model atmospheres from the Castelli & Kurucz (2003) grid. The stellar parameters derived from *The Cannon* are adopted to construct the stellar atmospheric model necessary for the synthesis – i.e.,  $T_{\text{eff}} = 3954 \text{ K}$ ,  $\log g = 1.16 \text{ dex}$ ,  $[\text{Fe}/\text{H}] = -0.7 \text{ dex}$  in this case. In the synthesis, we adjust the line profile to reproduce the resolution of *Gaia*-RVS ( $R \sim 11,500$ ) and the abundances of Zr, Ce, and Nd for those predicted by *The Cannon*:  $[\text{Zr}/\text{Fe}] = 0.27 \text{ dex}$ ,  $[\text{Ce}/\text{Fe}] = 0.31 \text{ dex}$ ,  $[\text{Nd}/\text{Fe}] = 0.81 \text{ dex}$  for this star. The line lists used to produce the synthetic spectra in the *Gaia*-RVS wavelength range are generated from *linemake*<sup>5</sup> (Placco et al. 2021) and shown in Table D1. The Ca II triplet lines are also included as a control sample, as explained later in this section.

We now convert the constructed synthetic spectrum to a set of weights using the following formula:

$$\hat{T}_i(v) = \frac{T_i(v)}{\sum T_i(v)} \quad (11)$$

This transformation ensures that the total sum of the templates equals one, with the largest weights allocated to the line positions.

To verify the presence of neutron-capture elements, we cross-correlated each template with a sub-sample of 2000 *Gaia*-RVS spectra randomly selected from a sample of stars with  $\chi^2 \approx 1$  between the *The Cannon* model estimates of flux and the observed flux. We

also searched for ionised Ca as a proof-of-concept for the application of the technique to our science case.

We cross-correlated over a range of  $-50$  to  $50 \text{ km s}^{-1}$  in  $1 \text{ km s}^{-1}$  intervals. It is important to note that *Gaia*-RVS spectra are known to have a fluctuating continuum level and occasionally contains aberrant data points. To normalise the cross-correlation function (CCF), we first masked the central region from  $-10$  to  $+10 \text{ km s}^{-1}$  to avoid the main absorption peak biasing the baseline. The remaining CCF was smoothed using a one-dimensional Gaussian filter to define the continuum, and the entire CCF was then divided by this smoothed profile. This rectified and flattened the continuum, enabling us to resolve the absorption features of the element under examination and allowing reliable detection even for weak lines. Each normalised CCF was then averaged over all stars to produce a one-dimensional cross-correlation function representing the total average line depth across the stars within our sample; for a more detailed description of the method used in this work, see Borsato et al. (2023).

To assess the robustness of the technique, we propagated the flux uncertainties of the RVS spectra through 1000 Monte Carlo realisations. In each iteration, the flux of each stellar spectrum was randomly sampled according to its associated measurement errors, assuming Gaussian noise, and the corresponding cross-correlation functions were recomputed and averaged. This procedure yielded 1000 realisations of the mean CCF, providing a rigorous estimate of the uncertainty and significance of the recovered absorption features. Our results are shown in Fig. 5, which displays the average CCF with its  $1\sigma$  significance region. As expected, the ionised Ca II peak shows a symmetrical curve and recovers the average line shape of the absorption to a high degree of significance, as indicated by the grey region in this figure; a less significant signal from the recovered line would produce a larger grey area throughout the absorption feature in that figure. Zr, Ce and Nd are well resolved, but at lower significance, suggesting that the flux probed by these lines is likely weak within the noise of the spectra and was only resolvable by combining lines. Nevertheless, the presence of peaks in Zr, Ce, and Nd (as well as Ca) indicates that typical RVS spectra contain measurable flux data for these elements. Combined with the pseudo-differential analysis, the cross-correlation test supports the interpretation that the *Gaia*-RVS spectra contain measurable neutron-capture information that can contribute to the *The Cannon*-inferred abundances. The resulting catalogue contains stellar label uncertainties for each star and element, allowing users to assess detection significance on a star-by-star basis as appropriate for their applications.

## 5 CHEMODYNAMICAL IDENTIFICATION OF GAIA-SAUSAGE-ENCELADUS (GSE) MEMBERS

We now turn to assessing the potential of our methods for tracing the chemodynamical evolution of the Milky Way by applying our results to a specific case – namely the identification of stars associated with *Gaia*-Sausage-Enceladus (GSE), a prominent accreted structure in the Milky Way’s stellar halo. In particular, we test whether stars selected solely on the basis of their chemical abundance patterns – as predicted by *The Cannon* – can be validated as probable GSE members based on their kinematic properties.

To compute the kinematic quantities of the stars and enable comparison with earlier GSE kinematic studies (particularly the analysis in Feuillet et al. 2021), we adopted the MWPotential2014 Galactic potential model from Bovy & Rix (2013) and Bovy (2015), assuming the solar position to be  $R_{\odot} = 8 \text{ kpc}$  and  $Z_{\odot} = 20.8 \text{ pc}$ . Corrections for the solar motion relative to the Local Standard of Rest were ap-

<sup>4</sup> Available at <https://www.as.utexas.edu/~chris/moog.html>

<sup>5</sup> <https://github.com/vmplacco/linemake>

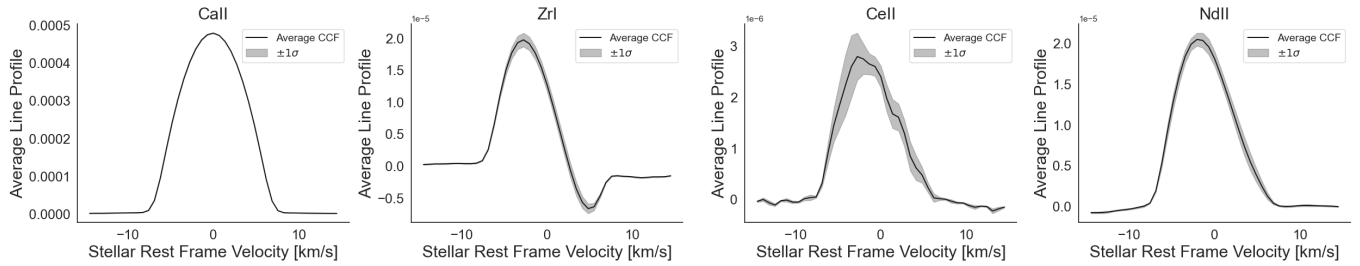


**Figure 5.** Cross-correlation detections of Ca II, Zr I, Ce II, and Nd II. The cross-correlation signal is shown as a black line with its  $1\sigma$  confidence interval marked as a grey region.

plied using the values  $U_{\odot} = 11.1 \text{ km s}^{-1}$ ,  $V_{\odot} = 12.24 \text{ km s}^{-1}$ , and  $W_{\odot} = 7.25 \text{ km s}^{-1}$  (Bennett & Bovy 2019). These corrections were used to transform heliocentric velocities to the Galactocentric frame, after which orbits were integrated and kinematic quantities were computed in the `MWPotential2014`, specifically the angular momentum along the  $z$ -axis ( $L_z$ ), the radial action ( $\sqrt{J_R}$ ), and the total orbital energy ( $E$ ). To construct a validation set, we cross-matched our sample of 314,010 stars (satisfying `flag_cannon = 0`) against the sample of 679 kinematically selected GSE members from Feuillet et al. (2021), where we found 86 probable GSE members common to both samples.

### 5.1 GSE membership probabilistic model

With the overlapping sample of 86 likely GSE members, we produced an empirical model based on the measured abundance labels to predict GSE membership. To achieve this, we designed a probabilistic forward model, coupled with a Markov Chain Monte Carlo (MCMC) sampler, which assigns a probability for GSE membership, trained on the abundance patterns of the 86 GSE stars obtained from Feuillet et al. (2021).

In addition to the training sample, we included 2000 stars randomly selected from the remaining non-overlapping *Gaia*-RVs sample. This ensured that the MCMC model would be able to distinguish GSE members from stars not identified in Feuillet et al. (2021). This comparison sample was chosen to provide a representative background population against which the abundance patterns of the known GSE members could be distinguished. We then used this model to find additional members using the respective stellar labels predicted by *The Cannon*. We adopted a logistic function from Cox (1958) to predict stellar GSE membership from the *Gaia*-RVs sample. The regression function used for this purpose has the following form:

$$P(Y = 1 | X) = \frac{1}{1 + e^{-(\beta_0 + \beta_1 X_1 + \beta_2 X_2 + \dots + \beta_n X_n)}} \quad (12)$$

Here,  $P(Y = 1 | X)$  is the probability that the dependent variable  $Y$  equals 1 given the input vector  $X$ ,  $\beta_0$  is the intercept (bias term), and  $\beta_1, \beta_2, \dots, \beta_n$  are the coefficients (weights) associated with the features  $X_1, X_2, \dots, X_n$ . This logistic equation produces a value between zero and one, enabling the creation of models that flag membership in a specific subset. The coefficient values obtained from Eq. 12 were used to create models indicating GSE membership.

The coefficients selected for regression were the abundance labels  $[\text{Fe}/\text{H}]$  and  $([\text{X}/\text{Fe}] + [\text{Fe}/\text{H}])$  – where  $X$  refers to the element in question ( $X = \text{Ti}, \text{Si}, \text{Ca}, \text{Ni}, \text{Zr}, \text{Nd}$  and  $\text{Ce}$ ) – to remove any co-linearity between the variables, necessary for producing robust predictor estimates (Hosmer et al. 2013). We then calculated the parameters of the logistic function using an MCMC sampler. The model

**Table 2.** Mean and uncertainty values for the coefficients obtained for each stellar abundance parameter used in the MCMC Model (see Section 5.1)

Parameter	$\beta_{\text{Fe}/\text{H}}$	$\beta_{\text{Ti}/\text{H}}$	$\beta_{\text{Si}/\text{H}}$	$\beta_{\text{Ca}/\text{H}}$	$\beta_{\text{Ni}/\text{H}}$	$\beta_{\text{Zr}/\text{H}}$	$\beta_{\text{Nd}/\text{H}}$	$\beta_{\text{Ce}/\text{H}}$	$\beta_{\text{const}}$
Mean	9.61	-5.89	-1.26	1.02	-10.61	1.29	0.89	-0.07	-4.61
Uncertainty	2.49	1.43	1.59	1.14	2.51	0.51	0.49	0.54	0.26

included eight free parameters, one constant term, and eight abundances. All abundance coefficients, including  $\beta_{\text{const}}$ ,  $\beta_{\text{Fe}/\text{H}}$ ,  $\beta_{\text{Ti}/\text{H}}$ ,  $\beta_{\text{Si}/\text{H}}$ ,  $\beta_{\text{Ca}/\text{H}}$ ,  $\beta_{\text{Ni}/\text{H}}$ ,  $\beta_{\text{Zr}/\text{H}}$ ,  $\beta_{\text{Nd}/\text{H}}$ , and  $\beta_{\text{Ce}/\text{H}}$ , were assigned uniform priors  $\mathcal{U}(-50, 50)$ . This set of broad priors enables an unbiased search for a well-fitting model. We sampled the prior distributions as before, using a No-U-Turn Sampler (Betancourt 2017) with the NumPyro (Bingham et al. 2018; Phan et al. 2019) and JAX (Bradbury et al. 2018) implementations. We sampled the posterior distribution of this model with 100,000 steps, taking 25,000 as burn-in and sampling the distributions for the remaining 75,000 (see Fig. 6). Our results show, in general, good posterior convergence and statistical significance, in addition to reasonable independence for most of the predictor values. The only exception to this is the strong correlation of  $[\text{Ni}/\text{H}]$  with  $[\text{Fe}/\text{H}]$ , which is expected since Ni is an Fe-peak element. We present the best-fitting parameter values along with their uncertainties in Table 2.

### 5.2 Interpreting the MCMC Framework for GSE Candidates

Using the coefficients derived for the model parameters (Table 2), we applied the regression function (Eq. 12) to each of the 314,010 stars (satisfying `flag_cannon = 0`) in our sample to estimate its GSE membership probability. Our approach is similar to Buder et al. (2022), who employed both chemical and dynamical selections using Gaussian Mixture Models to identify candidate GSE stars, demonstrating that purely chemical and purely dynamical selections yield overlapping but not identical samples.

In our analysis, we identified 3295 potential GSE candidate stars with membership probabilities  $P_{\text{mem}} > 55\%$ . Table E1 summarises the membership classification metrics for different probability thresholds, providing the basis for adopting 55% as the selected threshold. To assess the reliability of this threshold, we validated the regression model using the cross-matched MCMC training sample of 86 stars from Feuillet et al. (2021). At  $P_{\text{mem}} > 55\%$ , the model achieves high precision of 69% through maximised number of true positives relative to false positives, indicating that nearly two-thirds of stars predicted as GSE members above this threshold are expected to have correct probabilistic classifications. Based on this validation, we selected the 2289 high-confidence candidates ( $\sim 69\%$  of 3295) as our final sample of probable GSE members for further analysis.

To distinguish these 2289 probable GSE stars from the *in situ* halo and thick-disc populations, we constructed two comparison samples

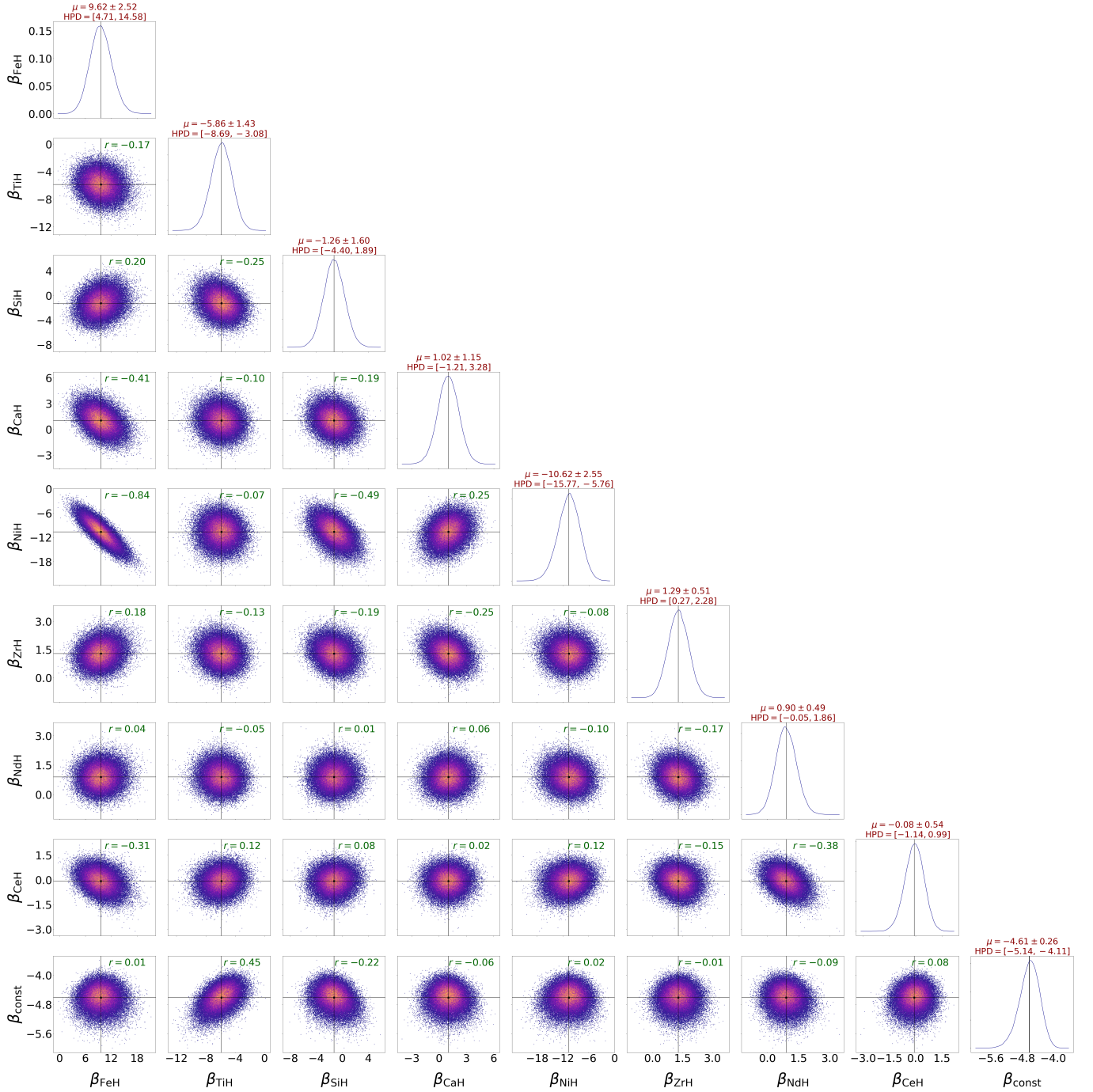


**Figure 6.** Posterior distributions and pairwise marginals for the MCMC model parameters (refer to Sec. 5.1). Each panel shows samples from the posterior distributions of the abundance ratio coefficients ( $\beta$  parameters) inferred from the model. The diagonal panels display the one-dimensional marginal posterior distributions for each parameter, with the mean ( $\mu$ ) and standard deviation ( $\sigma$ ) indicated, together with the 95% Highest Posterior Density (HPD) interval. The off-diagonal hexbin panels illustrate the pairwise relationships between parameters, where colour intensity indicates the density of posterior samples. Annotated values of  $r$  denote the Pearson correlation coefficient between each pair of parameters, quantifying the strength and direction of their linear dependence ( $r = 1$ : perfect positive correlation;  $r = -1$ : perfect negative correlation;  $r = 0$ : no linear correlation). Together, these visualisations highlight both the marginal uncertainties and inter-parameter correlations within the inferred posterior distributions.

of probable non-GSE stars. The first sample includes *in situ* halo stars, with  $[\text{Fe}/\text{H}] < -0.8$  dex and  $[\text{Ti}/\text{Fe}] > 0.25$  dex, comprising chemically older,  $\alpha$ -enhanced populations formed within the Milky Way. These stars were further selected to have angular momenta in the range  $-1500 < L_z$  ( $\text{kpc km s}^{-1}$ )  $< 1500$  and orbital eccentricities  $0.5 < e < 0.8$ , following kinematic boundaries commonly

adopted to separate accreted and *in situ* halo components (see e.g. Belokurov et al. 2018; Koppelman et al. 2019, 2018; Naidu et al. 2020; Feuillet et al. 2021). The roughly symmetric range around  $L_z \approx 0$   $\text{kpc km s}^{-1}$  isolates stars on low-angular-momentum, moderately eccentric orbits typical of the *in situ* halo, while excluding the strongly radial GSE debris. For the non-GSE thick-disc sample,

we adopted the same chemical criteria as for the *in situ* halo, but required  $L_z > 0$  kpc km s<sup>-1</sup> and  $e < 0.5$  to select stars on more circular, prograde, rotationally supported orbits characteristic of the Galactic disc. This kinematic separation increases the likelihood that the comparison populations represent stars formed within the Milky Way, enabling a better assessment of chemical and dynamical distinctions between *in situ* and accreted halo components. We also note that, primarily due to their lower metallicities, GSE stars can be more readily distinguished from the thin-disc population.

Using *The Cannon*-predicted chemical abundances, we examined their pairwise abundance distributions across four distinct stellar samples: (a) the sample of 2289 high-confidence probable GSE members with membership probabilities  $P_{\text{mem}} > 55\%$ ; (b) the sample of our probable non-GSE halo stars selected based on the criteria outlined previously; (c) the sample of non-GSE thick-disc stars, also defined as described earlier; and (d) a reference sample of the 86 GSE stars common to our catalogue of RVS giants and the kinematically selected GSE sample from [Feuillet et al. \(2021\)](#) (see Fig. F1 for all the pairwise abundance distributions). Visual inspection of these distributions – subsequently validated using a Random Forest classifier – reveals that the abundance ratios [Ca/Ti], [Ti/Ce], and [Nd/Zr] exhibit similar trends in both the predicted GSE sample and the reference GSE sample, while being distinct from those of the thick-disc and halo stellar populations. These differences are further highlighted in Fig. 7, which focuses on the pairwise correlations of the selected abundance ratios. The distributions of peak population densities differ notably across the samples, emphasising the power of these abundance ratios for identifying probable GSE candidates.

We also show kernel density estimates (KDEs) of the abundance ratios [Ca/Ti], [Ti/Ce], and [Nd/Zr] for our sample of 2289 GSE candidate stars and the chemodynamically selected comparison sample of non-GSE halo stars in Fig. 8. For each abundance ratio, we indicate the location of the GSE KDE peak and its associated  $1\sigma$  interval, defined by the 16<sup>th</sup> and 84<sup>th</sup> percentiles of the GSE distribution. Within these GSE  $1\sigma$  intervals, we find that 376 (~29%), 283 (~22%), and 462 (~36%) of the halo stars fall within the  $1\sigma$  intervals for [Ca/Ti], [Ti/Ce], and [Nd/Zr], respectively. These abundance ratios show intriguing differences among individual  $\alpha$ - and neutron-capture elements. The higher [Ca/Ti] ratios observed for our GSE candidates relative to the *in situ* halo and thick-disc populations may indicate subtle variations within the explosive  $\alpha$ -element group ([Horta & Ness 2025](#)). Similarly, the lower [Ti/Ce] and slightly higher [Nd/Zr] in our sample may reflect intra-process variations within the neutron-capture domain, arising from differing contributions of slow- and rapid-process enrichment channels. While [Horta & Ness \(2025\)](#) focused on hydrostatic versus explosive  $\alpha$ -element production, our results suggest that analogous intra-process variations may also exist among neutron-capture elements in accreted systems such as GSE, highlighting subtle internal differences within element families linked to their star-formation and chemical-enrichment histories, a topic which warrants future exploration.

These patterns are broadly consistent with earlier findings for Galactic stellar populations. For example, [Nissen & Schuster \(2010\)](#) identified two distinct halo populations based on  $[\alpha/\text{Fe}]$  ratios, with low- $\alpha$  stars exhibiting signatures of slower star formation and likely accreted origin and high- $\alpha$  stars reflecting rapid *in situ* enrichment. Similarly, [Fishlock et al. \(2017\)](#) showed that low- $\alpha$  halo stars display characteristic neutron-capture abundance patterns, such as higher [Ba/Y] and lower [Y/Eu], indicative of contributions from low-metallicity AGB stars. Our observed differences in [Ca/Ti], [Ti/Ce], and [Nd/Zr] among GSE candidates versus *in situ* populations are conceptually similar to these studies, emphasising the diagnostic

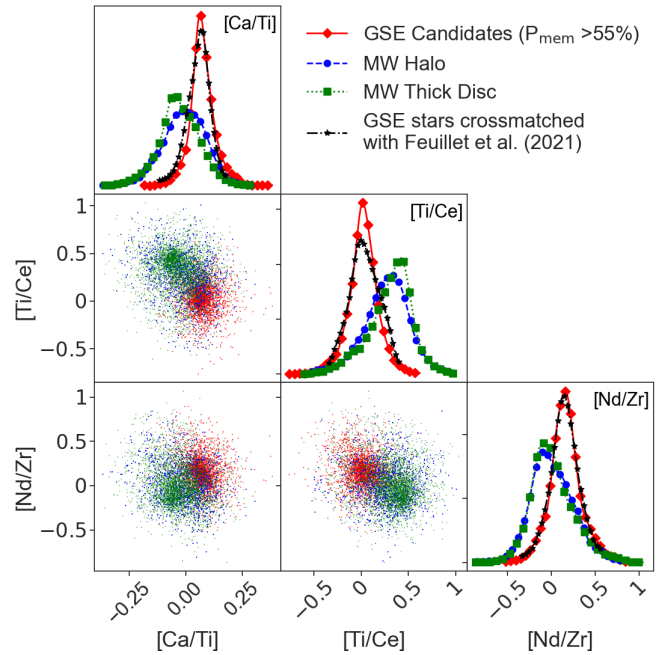


**Figure 7.** Distributions and pairwise correlations of the abundance ratios—[Ca/Ti], [Ti/Ce], and [Nd/Zr]—for four distinct stellar populations: 2289 probable GSE candidate stars with  $P_{\text{mem}} > 55\%$  (red); halo stars (blue), thick disc stars (green), and a cross-match of 86 GSE stars from [Feuillet et al. 2021](#) with our catalogue of 314,010 *Gaia*-RVS stars (black) satisfying `flag_cannon = 0`. Diagonal panels display Kernel Density Estimates of the one-dimensional distributions, while the lower off-diagonal panels show corresponding two-dimensional scatter plots. The relative chemical distributions for these the ratios ([Ca/Ti], [Ti/Ce], and [Nd/Zr]) highlight distinct signatures between accreted (GSE) and *in situ* (halo and thick disc) populations, supporting the use of these abundance ratios as discriminants of stellar origin in the Milky Way halo.

power of intra-process abundance ratios to distinguish accreted from *in situ* stars.

Our chemical-abundance-based selection of GSE candidates complements alternative approaches employed in the literature. For instance, [Hawkins et al. \(2015\)](#) and [Das et al. \(2020\)](#) utilised abundance planes such as [Al/Fe] versus [Mg/Mn] to separate accreted from *in situ* populations, while [Buder et al. \(2022\)](#) employed [Na/Fe] versus [Mg/Mn] in combination with Gaussian Mixture Models for the same purpose. Although these methods rely on different chemical tracers, they share the underlying principle of using element ratios sensitive to star formation history and nucleosynthetic pathways to distinguish accreted substructures. Hence our approach, based on [Ca/Ti], [Ti/Ce], and [Nd/Zr], provides a complementary perspective, particularly highlighting intra-process differences among  $\alpha$ - and neutron-capture elements.

To further investigate the overlap of our sample of 2289 GSE candidates with the dynamically selected GSE sample of [Feuillet et al. \(2021\)](#), we applied kinematic criteria of  $-500 \leq L_z$  (kpc km s<sup>-1</sup>)  $\leq 500$  and  $30 \leq \sqrt{J_r}$  (kpc<sup>1/2</sup> km<sup>1/2</sup> s<sup>-1</sup>)  $\leq 55$ . Applying these cuts to the initial sample resulted in a sample selection of 286 stars that satisfy both our probabilistic chemical selection and the dynamical criteria.

Fig. 9 shows the normalised distributions of eight elemental abundance ratios ([Fe/H], [Ti/Fe], [Ca/Fe], [Ni/Fe], [Si/Fe], [Nd/Fe], [Zr/Fe], and [Ce/Fe]) for four samples: (i) the chemically selected high-confidence GSE candidates ( $P_{\text{mem}} > 55\%$ , 2289 stars), (ii) the

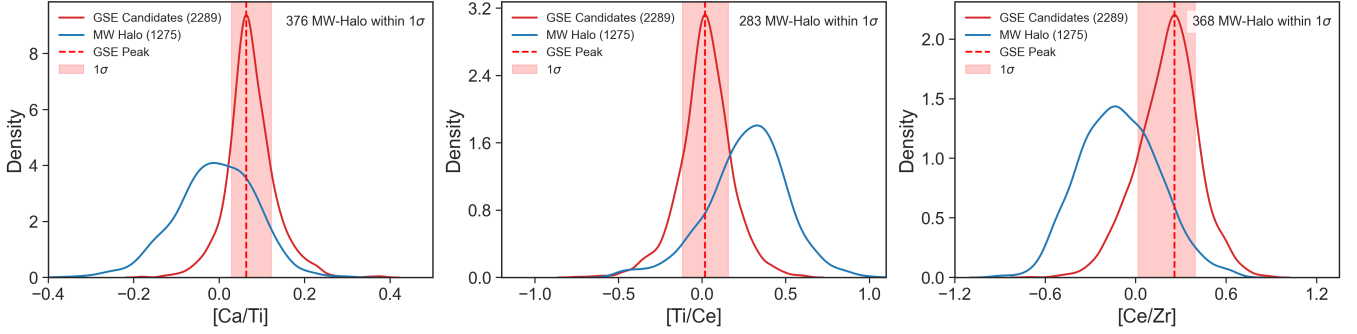


**Figure 8.** Kernel density estimates of the selected chemical abundance ratios— $[\text{Ca}/\text{Ti}]$ ,  $[\text{Ti}/\text{Ce}]$ , and  $[\text{Nd}/\text{Zr}]$ —for 2289 GSE candidate stars (red), and the Milky Way halo stars (blue) restricted to  $[\text{Fe}/\text{H}] < -0.8$ ,  $[\text{Ti}/\text{Fe}] > 0.25$  dex,  $0.5 < e < 0.8$ , and  $|L_z| < 1500$  kpc km s $^{-1}$ . For each abundance ratio, the peak of the distribution (dashed line) and  $1\sigma$  interval (16<sup>th</sup>–84<sup>th</sup> percentile, shaded region) are indicated. Annotations in each panel report the number of halo stars falling within the GSE  $1\sigma$  range. These comparisons highlight systematic chemical distinctions between the GSE and the *in situ* halo, reflecting different nucleosynthetic enrichment histories.

subset of 286 stars also satisfying dynamical criteria [ $-500 \leq L_z$  (kpc km s $^{-1}$ )  $\leq 500$  and  $30 \leq \sqrt{J_r}$  (kpc $^{1/2}$  km $^{1/2}$  s $^{-1}$ )  $\leq 55$ ], and (iii–iv) GALAH DR3 and DR4 abundances for the GSE sample from [Buder et al. \(2022\)](#) (using their recommended membership  $> 45\%$ , based on chemical selection). The coloured lines represent the relative distributions of each sample; the inset legend in each panel reports the median and 16<sup>th</sup>–84<sup>th</sup> percentile spreads (dex). We also calculate the median abundances for all the elements analysed in Table 3. We show that the 286 chemodynamically selected stars exhibit median abundances that closely match those of the full chemical sample of 2289 GSE candidates, demonstrating that the kinematic cut does not introduce notable bias in the overall chemical patterns. The median abundances from GALAH DR4 are generally consistent with both the chemically selected and the chemodynamically selected samples, reflecting the fact that *The Cannon* was trained using GALAH DR4 labels as the reference in the model. In contrast, the GALAH DR3 abundances show systematic offsets and exhibit broader distributions or slightly different medians for the  $\alpha$ - ( $[\text{Ca}/\text{Fe}]$ ,  $[\text{Ti}/\text{Fe}]$ ) and neutron-capture elements ( $[\text{Nd}/\text{Fe}]$ ,  $[\text{Zr}/\text{Fe}]$ ,  $[\text{Ce}/\text{Fe}]$ ). These differences likely reflect the variations in label calibration and the analysis methodologies adopted in GALAH DR3 versus DR4.

For the sample of 286 GSE candidates, consisting exclusively of RVS giant stars, *The Cannon*-predicted metallicity is obtained as  $[\text{Fe}/\text{H}] = -1.56^{+0.23}_{-0.24}$  dex. We note that this result reflects a more metal-poor population compared to previously reported literature values for GSE, such as  $\sim (-1.17 \pm 0.34)$  dex in [Feuillet et al. \(2020\)](#),  $\sim (-1.15)$  dex in [Feuillet et al. \(2021\)](#) and  $(-1.15^{+0.24}_{-0.33})$  dex in [Naidu et al. \(2020\)](#). A possible explanation for this metallicity difference is the exclusive use of giant stars in our sample, as GSE membership probabilities may be higher due to better chemical distinctions from the *in situ* halo field at low metallicity; incorporating GSE dwarfs in the sample would likely yield a higher mean metallicity. This can be seen in Fig. 3 of [Ernandes et al. \(2024\)](#), where GSE giants display a more metal-poor distribution relative to the GSE dwarfs within the same primary sample.

To visualise how our chemically selected GSE candidates occupy dynamical space, Fig. 10 presents the distribution of the 2289 probable GSE stars in the  $L_z$ – $\sqrt{J_R}$  and  $L_z$ – $E$  planes. The majority of these stars cluster around low angular momentum ( $L_z \approx 0$ ) and moderate-to-high  $\sqrt{J_R}$  and eccentricities, consistent with the highly radial, weakly rotating orbits characteristic of GSE debris. This behaviour is in agreement with previous studies showing that the GSE progenitor was accreted on a predominantly radial orbit, leaving behind

stars with little net rotation and elevated orbital energies ([Belokurov et al. 2018](#); [Feuillet et al. 2021](#); [Naidu et al. 2021](#)). Note that, as our selection is based purely on chemical abundances, there are stars distributed across a fairly broad range of dynamical space. While a substantial fraction lies within the canonical GSE region defined by low  $L_z$  and high radial action, a subset of stars extends beyond these bounds, potentially reflecting the natural diversity in the orbital properties of the accreted debris, as well as perhaps some degree of contamination by stars of different origins. If intrinsic to GSE stars, the spread could result from variations in the progenitor’s structure, the range of energies and angular momenta at infall, and subsequent dynamical evolution within the Milky Way potential. Recent reanalyses of the sample from [Nissen & Schuster \(2010\)](#) provide further evidence for GSE debris spanning a broad kinematic range, with chemical tracers such as  $[\text{Al}/\text{Fe}]$  identifying GSE-like stars across varied orbital energies, and indications of multiple progenitor passages producing an Fe– $E$  gradient ([Skúladóttir et al. 2025](#); [Ernandes et al. 2025](#); [Berni et al. 2026](#)). This supports the interpretation that the kinematic diversity in our chemically selected sample is largely intrinsic to GSE. Overall, these results suggest that the chemical selection broadly traces the GSE debris population, while dynamical refinement identifies a subset that is more tightly concentrated in the traditionally defined GSE region.

## 6 CONCLUSIONS

Our study demonstrates the ability of *The Cannon* to transfer high-resolution GALAH DR4 stellar labels ( $R \approx 28,000$ ) to lower-resolution *Gaia* DR3 RVS spectra ( $R \approx 11,500$ ), enabling inference of stellar parameters ( $T_{\text{eff}}$ ,  $\log g$ , and  $v \sin i$ ) and a broad range of elemental abundances, including  $[\text{Fe}/\text{H}]$ ,  $[\text{Ca}/\text{Fe}]$ ,  $[\text{Si}/\text{Fe}]$ ,  $[\text{Ni}/\text{Fe}]$ , and  $[\text{Ti}/\text{Fe}]$ , for a sample of 357,415 RVS giant stars (using  $\log g < 3.5$  dex from the catalogue in [Das et al. 2025b](#)). Notably, the model also predicts neutron-capture element abundances such as  $[\text{Zr}/\text{Fe}]$ ,  $[\text{Ce}/\text{Fe}]$ , and  $[\text{Nd}/\text{Fe}]$  with low scatter. Twelve-fold cross-validation on the training set confirms internal consistency, with RMSE values of  $\sim 70$  K ( $T_{\text{eff}}$ ),  $\sim 0.14$  dex ( $\log g$ ),  $\leq 0.10$  dex for most abundances and  $\sim 0.15$  dex for neutron-capture elements. Of these, 314,010 stars satisfy `flag_cannon = 0`, representing a high-fidelity subsample within the training label-space bounds.

To independently assess the detectability of neutron-capture features in the RVS spectra, we carried out a pseudo-differential analysis

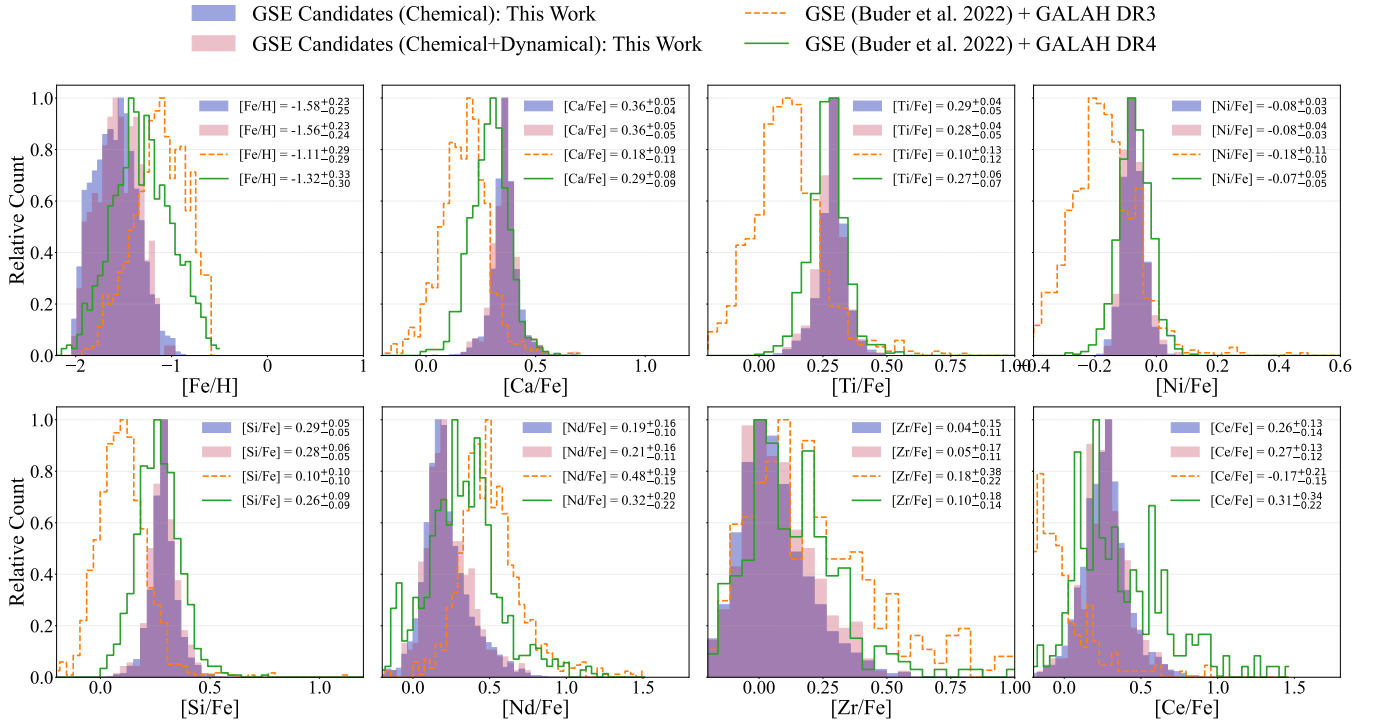


**Figure 9.** Each panel shows the normalized histogram of a given element ratio ([Fe/H], [Ti/Fe], [Ca/Fe], [Ni/Fe], [Si/Fe], [Nd/Fe], [Zr/Fe], [Ce/Fe]) for four samples of GSE stars: 2289 GSE candidates selected chemically in our work ( $P_{\text{mem}} > 55\%$ ) marked with blue; a subset of 286 GSE candidates selected chemically in our sample ( $P_{\text{mem}} > 55\%$ ) and satisfying the dynamical conditions from [Feuillet et al. \(2021\)](#) [ $-500 \leq L_z$  (kpc km s $^{-1}$ )  $\leq 500$  and  $30 \leq \sqrt{J_r}$  (kpc $^{1/2}$  km $^{1/2}$  s $^{-1}$ )  $\leq 55$ ] marked with pink; and the GALAH DR3 and DR4 elemental abundances cross-matched with the GSE sample from [Buder et al. \(2022\)](#), satisfying membership  $> 45\%$  for [Na/Fe] versus [Mg/Mn] marked with orange and green respectively. Coloured lines indicate the relative distribution for each dataset. The inset legend in each panel gives the median value with 16<sup>th</sup>–84<sup>th</sup> percentile spreads (dex) for each sample within each elemental space. The vertical axis represents the relative frequency, normalised to the maximum of each distribution. The global legend above the panels identifies the datasets.

**Table 3.** Median elemental abundances (dex) with 16<sup>th</sup>–84<sup>th</sup> percentile spreads for eight elements ([Fe/H], [Ti/Fe], [Ca/Fe], [Ni/Fe], [Si/Fe], [Nd/Fe], [Zr/Fe], [Ce/Fe]) in four GSE samples: (1) 2289 chemically selected GSE candidates ( $P_{\text{mem}} > 55\%$ ); (2) 286 GSE candidates selected using both chemical and dynamical criteria [ $P_{\text{mem}} > 55\%$ ,  $-500 \leq L_z$  (kpc km s $^{-1}$ )  $\leq 500$ , and  $30 \leq \sqrt{J_r}$  (kpc $^{1/2}$  km $^{1/2}$  s $^{-1}$ )  $\leq 55$ ]; (3) and (4) denote GSE stars identified by [Buder et al. \(2022\)](#) based on their [Na/Fe]–[Mg/Mn] distribution (membership probability  $> 45\%$ ), with elemental abundances taken from GALAH DR3 and DR4, respectively.

Element	GSE Candidates (Chemical) <sup>1</sup>	GSE Candidates (Chemical+Dynamical) <sup>2</sup>	GALAH DR3 GSE <sup>3</sup>	GALAH DR4 GSE <sup>4</sup>
[Fe/H]	$-1.58^{+0.23}_{-0.25}$	$-1.56^{+0.23}_{-0.24}$	$-1.11^{+0.29}_{-0.29}$	$-1.32^{+0.33}_{-0.30}$
[Ca/Fe]	$0.36^{+0.05}_{-0.04}$	$0.36^{+0.05}_{-0.05}$	$0.18^{+0.09}_{-0.11}$	$0.29^{+0.08}_{-0.09}$
[Ti/Fe]	$0.29^{+0.04}_{-0.05}$	$0.28^{+0.04}_{-0.05}$	$0.10^{+0.13}_{-0.12}$	$0.27^{+0.06}_{-0.07}$
[Ni/Fe]	$-0.08^{+0.03}_{-0.03}$	$-0.08^{+0.04}_{-0.03}$	$-0.18^{+0.11}_{-0.10}$	$-0.07^{+0.05}_{-0.05}$
[Si/Fe]	$0.29^{+0.05}_{-0.05}$	$0.28^{+0.06}_{-0.05}$	$0.10^{+0.10}_{-0.10}$	$0.26^{+0.09}_{-0.09}$
[Nd/Fe]	$0.19^{+0.16}_{-0.10}$	$0.21^{+0.16}_{-0.11}$	$0.48^{+0.19}_{-0.15}$	$0.32^{+0.20}_{-0.22}$
[Zr/Fe]	$0.04^{+0.15}_{-0.11}$	$0.05^{+0.17}_{-0.11}$	$0.18^{+0.38}_{-0.22}$	$0.10^{+0.18}_{-0.14}$
[Ce/Fe]	$0.26^{+0.13}_{-0.14}$	$0.27^{+0.13}_{-0.12}$	$-0.17^{+0.21}_{-0.15}$	$0.31^{+0.34}_{-0.22}$

of two stars with similar stellar parameters but different [Nd/Fe], illustrating the small (but noticeable) flux variations in the Nd lines. We also applied a multi-line cross-correlation technique to a representative sub-sample of 2000 RVS giants satisfying a reduced chi-squared value ( $\chi^2$ )  $\approx 1$  between the *The Cannon* model estimates of flux and the observed RVS spectral flux. This latter approach showed well-defined peaks in the cross-correlation functions for Zr, Ce, and Nd absorption features, supporting the presence of measurable abundance information in the spectral range. Combined together, these

results support the reliability of *The Cannon*'s abundance predictions for the neutron-capture elements.

Applying the results of our analysis to the stellar populations of the Milky Way, we used an empirical, abundance-based framework optimised with an MCMC sampler to identify probable GSE members. The training sample consisted of 86 stars overlapping between our catalogue and the kinematically selected GSE sample from [Feuillet et al. \(2021\)](#), supplemented by a sample of 2000 randomly selected non-GSE stars to ensure distinction from *in situ* populations. This

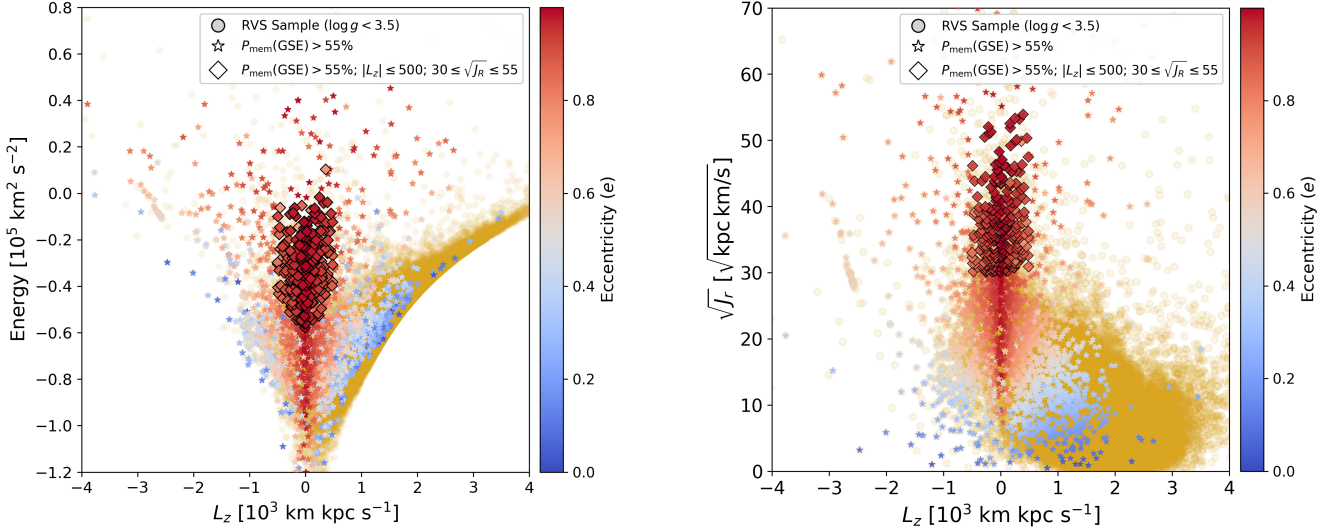


**Figure 10.** Kinematic distribution of red giant stars analyzed with *The Cannon*. **Left:** Total orbital energy ( $E$ ) versus angular momentum ( $L_z$ ). The golden coloured-points show the RVS sample of 314,010 RVS giants (`flag_cannon = 0`). Star-shaped markers denote probable GSE members with  $P_{\text{mem}} > 55\%$ , selected using the abundance-based MCMC model. Diamond-shaped markers show the subset of stars that also satisfy the dynamical cuts from [Feuillet et al. \(2021\)](#), namely  $|L_z| \leq 500$  kpc km s $^{-1}$  and  $30 \leq \sqrt{J_R}$  (kpc $^{1/2}$  km $^{1/2}$  s $^{-1}$ )  $\leq 55$ . **Right:** Radial action ( $\sqrt{J_R}$ ) versus  $L_z$  for the same sample of stars. The various markers denote the same objects as it was in the left panel. Colour bars indicate eccentricity ( $e$ ) for the probable GSE candidates only.

**Table 4.** Median dynamical properties with 16<sup>th</sup> and 84<sup>th</sup> percentile uncertainties for the chemically and chemodynamically selected GSE Candidates.

Parameter	GSE Candidates (Chemical) <sup>1</sup>	GSE Candidates (Chemical+Dynamical) <sup>2</sup>
$\sqrt{J_R}$ ( $\sqrt{\text{kpc km s}^{-2}}$ )	19.37 $^{+8.98}_{-14.02}$	35.82 $^{+4.27}_{-7.39}$
$L_x$ (kpc km s $^{-1}$ )	36.77 $^{+316.20}_{-330.20}$	11.58 $^{+225.12}_{-232.74}$
$L_y$ (kpc km s $^{-1}$ )	-35.24 $^{+533.26}_{-545.86}$	-19.57 $^{+572.98}_{-507.89}$
$L_z$ (kpc km s $^{-1}$ )	170.56 $^{+660.80}_{-800.08}$	-12.72 $^{+238.50}_{-279.61}$
$E$ ( $10^5$ km $^2$ s $^{-2}$ )	-0.57 $^{+0.19}_{-0.29}$	-0.33 $^{+0.11}_{-0.15}$
$V_R$ (km s $^{-1}$ )	1.55 $^{+154.64}_{-158.05}$	85.99 $^{+378.11}_{-204.34}$
$V_\phi$ (km s $^{-1}$ )	28.21 $^{+107.40}_{-122.94}$	-1.66 $^{+29.67}_{-37.83}$
$V_z$ (km s $^{-1}$ )	-4.91 $^{+96.87}_{-92.06}$	2.43 $^{+104.03}_{-110.94}$
$e$ (eccentricity)	0.70 $^{+0.33}_{-0.23}$	0.95 $^{+0.05}_{-0.04}$

<sup>1</sup> GSE Candidates with  $P_{\text{mem}} > 55\%$  (2289 stars).

<sup>2</sup> GSE Candidates with  $P_{\text{mem}} > 55\%$  and satisfying  $|L_z| \leq 500$  kpc km s $^{-1}$  and  $30 \leq \sqrt{J_R}$  (kpc $^{1/2}$  km $^{1/2}$  s $^{-1}$ )  $\leq 55$  (286 stars).

model produced membership probabilities for the 314,010 RVS giants (`flag_cannon = 0`), from which 3295 stars exceeded a probability threshold of 55%. Accounting for the estimated precision of approximately 69% at this threshold (i.e., considering both true and false positives), we selected 2289 stars with the highest probabilities ( $\approx 69\%$  of 3295) as our high-confidence probable GSE candidates.

On comparing the chemical abundance ratios of these 2289 probable GSE candidates to that of *in situ* Milky Way halo and thick-disc comparison samples, the abundance ratios [Ca/Ti], [Ti/Ce], and [Nd/Zr] showed distinct distributions between the GSE candidates and *in situ* populations, highlighting differences in nucleosynthetic histories. This was further validated by a Random Forest classifier, confirming that these abundance ratios can potentially separate the chemically selected GSE stars from *in situ* halo and disc stars. These

patterns are conceptually consistent with previous studies of accreted populations and halo chemistry, such as [Nissen & Schuster \(2010\)](#) and [Fishlock et al. \(2017\)](#), and are broadly aligned with previous chemodynamical selections of GSE stars ([Buder et al. 2022](#)).

We further examined the dynamical properties of these 2289 GSE candidates using the MWPotential2014 Galactic potential model from [Bovy & Rix \(2013\)](#) and [Bovy \(2015\)](#). The majority of the 2289 GSE candidates occupy around low angular momentum ( $L_z \approx 0$ ) and moderate-to-high radial action ( $\sqrt{J_R}$ ), corresponding to the highly radial, weakly rotating orbits characteristic of GSE debris. This is in agreement with previous studies suggesting that the GSE progenitor was accreted on a predominantly radial orbit, leaving behind stars with little net rotation and elevated orbital energies ([Belokurov et al. 2018](#); [Naidu et al. 2021](#)). The stars are distributed across a broad dynamical range, potentially reflecting natural diversity in the progenitor’s orbital energy, angular momentum, and subsequent evolution in the Milky Way potential, as well as possibly indicating some degree of contamination from stars having different origins. Applying dynamical cuts from [Feuillet et al. \(2021\)](#) [ $-500 \leq L_z$  (kpc km s $^{-1}$ )  $\leq 500$  and  $30 \leq \sqrt{J_R}$  (kpc $^{1/2}$  km $^{1/2}$  s $^{-1}$ )  $\leq 55$ ] identifies 286 stars within the canonical GSE region, showing that the purely chemical selection broadly traces the debris, while the dynamical selection defines a more concentrated subset. The mean predicted metallicity of this dynamically selected subset is obtained as  $[\text{Fe}/\text{H}] = -1.56^{+0.23}_{-0.24}$  dex, a relatively more metal poor population as compared to the existing literature sources ([Feuillet et al. 2020, 2021](#); [Naidu et al. 2020](#)). This is likely due to the exclusive inclusion of RVS giants in our sample which yields more metal poor-population. This can also be seen in fig. 3 of [Ernandes et al. \(2024\)](#), where the GSE giants displayed a more metal-poor distribution as compared to the GSE dwarf population. Table 4 presents the kinematic properties calculated for the samples of chemically (2289) and chemodynamically (286) selected GSE candidates.

Overall, our results demonstrate that combining data-driven chemical abundance inference with probabilistic classification and dynamical validation provides a robust and scalable framework for identi-

fying accreted stellar populations. *The Cannon*, trained on high-resolution reference data, can reliably infer both  $\alpha$ - and neutron-capture element abundances for large samples of moderate-resolution spectra when complemented by appropriate statistical tests. Chemical selection criteria effectively identify probable GSE stars, while dynamical comparisons provide the kinematic context necessary to interpret the orbital properties of these accreted populations. Although these abundance estimates are robust at the population level, results for individual stars (particularly those near the edges of the parameter space or with lower SNR) may carry higher uncertainties.

The resulting chemical patterns of the GSE candidates – involving abundance ratios of a combination of alpha and neutron-capture elements, in our case [Ca/Ti], [Ti/Ce] and [Nd/Zr] – provide a statistically robust view of the stellar populations accreted during this merger event. While other elemental ratios have been used to distinguish between accreted and *in situ* populations (e.g., Hawkins et al. 2015; Das et al. 2020; Buder et al. 2022; ErnanDES et al. 2025), the addition of neutron-capture elements provides additional constraints on the detailed chemical evolution of GSE. This approach can be readily extended to characterise other halo substructures both in *Gaia*-RVS data (e.g., Das et al. *in prep.*) and in upcoming large-scale spectroscopic surveys. A key question to be addressed in future work is whether the specific elemental abundance ratios we find to be characteristic of GSE are distinct from those associated with other accretion events. With the approaching advent of *Gaia* DR4, which will include over 200 million RVS spectra – more than a hundredfold increase over DR3 – this methodology will enable the chemodynamical mapping of a significant sample of the Galaxy’s stellar populations, allowing us to trace the Milky Way’s accretion history in unprecedented detail, and thereby help in disentangling the complex process of Galactic assembly.

## ACKNOWLEDGEMENTS

PBD is supported by the Australian Commonwealth Government Research Training Program (RTP) Scholarship (<https://doi.org/10.82133/C42F-K220>). PBD acknowledges support from the Astronomical Society of Australia (ASA) Student Travel Grant 2025 (<https://asa.astronomy.org.au/prizes-and-grants/the-student-travel-grant/>), the Macquarie University Postgraduate Research Fund (PGRF) 2025, and the European Southern Observatory (ESO) Garching Early Career Scientific Visitor Programme 2025. Parts of this research were supported by the Australian Research Council (ARC) Centre of Excellence for All Sky Astrophysics in 3 Dimensions (ASTRO-3D), through project number CE170100013.

AMG, DBZ, GFL, and SLM acknowledge support from the ARC through Discovery Project DP220102254. DF acknowledges funding from the Swedish Research Council grant 2022-03274. TN acknowledges support from the Knut and Alice Wallenberg Foundation. SLM acknowledges support from the UNSW Scientia Fellows Program. DS is supported by the Australian Research Council Discovery Project DP250104267. PBD thanks Anish Amarsi and Madeleine McKenzie for helpful discussions related to this work. The authors also thank the anonymous reviewer for the valuable comments and suggestions.

This work has used the Fourth Data Release of the GALAH Survey. The GALAH survey is based on data acquired through the Australian Astronomical Observatory, under the programmes: A/2013B/13 (The GALAH pilot survey); A/2014A/25, A/2015A/19, A2017A/18 (The GALAH survey, Phase 1); A2018A/18 (Open

clusters with HERMES); A2019A/1 (Hierarchical star formation in Ori OB1); A2019A/15 (The GALAH survey, Phase 2); A/2015B/19, A/2016A/22, A/2016B/10, A/2017B/16, A/2018B/15 (The HERMES-TESS programme); and A/2015A/3, A/2015B/1, A/2015B/19, A/2016A/22, A/2016B/12, A/2017A/14 (The HERMES K2-follow-up programme). We acknowledge the traditional owners of the land on which the Anglo-Australian Telescope stands, the Gamilaraay people, and pay our respects to elders past and present. This paper includes data that has been provided by AAO Data Central (<https://datacentral.org.au/>).

This work has made use of the data from the European Space Agency (ESA) mission *Gaia* (<https://www.cosmos.esa.int/gaia>), processed by the *Gaia* Data Processing and Analysis Consortium (DPAC, <https://www.cosmos.esa.int/web/gaia/dpac/consortium>). Funding for the DPAC has been provided by national institutions, in particular the institutions participating in the *Gaia* Multilateral Agreement.

This paper also utilised NASA’s Astrophysics Data System (ADS) bibliographic services, as well as the open-source Python packages ASTROPY (<http://www.astropy.org>) (Astropy Collaboration et al. 2013, 2018, 2022), NUMPY (Harris et al. 2020), PANDAS (McKinney 2010), MATPLOTLIB (Hunter 2007), and TOPCAT (Taylor 2005, 2011).

## DATA AVAILABILITY

The data underlying this article will be available at the CDS via anonymous FTP to <https://cdsarc.u-strasbg.fr> (130.79.128.5) or via the VizieR catalogue service at <https://cdsarc.cds.unistra.fr/viz-bin/cat/J/MNRAS/Vol/Page>.

## REFERENCES

- Astropy Collaboration et al., 2013, *A&A*, **558**, A33  
 Astropy Collaboration et al., 2018, *AJ*, **156**, 123  
 Astropy Collaboration et al., 2022, *ApJ*, **935**, 167  
 Belokurov V., Erkal D., Evans N. W., Koposov S. E., Deason A. J., 2018, *MNRAS*, **478**, 611  
 Bennett M., Bovy J., 2019, *MNRAS*, **482**, 1417  
 Berni L., Palla M., Magrini L., Spina L., 2026, *A&A*, **707**, A242  
 Betancourt M., 2017, *arXiv e-prints*, p. arXiv:1706.01520  
 Bingham E., et al., 2018, *arXiv e-prints*, p. arXiv:1810.09538  
 Borsato N. W., Hoeijmakers H. J., Prinoth B., Thorsbro B., Forsberg R., Kitzmann D., Jones K., Heng K., 2023, *A&A*, **673**, A158  
 Bovy J., 2015, *ApJS*, **216**, 29  
 Bovy J., Rix H.-W., 2013, *ApJ*, **779**, 115  
 Bradbury J., Frostig R., Hawkins P., Johnson M. J., Leary C., Maclaurin D., Wanderman-Milne S., 2018, JAX: Composable transformations of Python+NumPy programs, <https://github.com/google/jax>  
 Brzeski J., Case S., Gers L., 2011, in Hatheway A. E., ed., Society of Photo-Optical Instrumentation Engineers (SPIE) Conference Series Vol. 8125, Optomechanics 2011: Innovations and Solutions. p. 812504, doi:10.1117/12.896389  
 Buder S., et al., 2018, *MNRAS*, **478**, 4513  
 Buder S., et al., 2021, *MNRAS*, **506**, 150  
 Buder S., et al., 2022, *MNRAS*, **510**, 2407  
 Buder S., et al., 2025, *Publ. Astron. Soc. Australia*, **42**, e051  
 Carrillo A., Hawkins K., Jofré P., de Brito Silva D., Das P., Lucey M., 2022, *MNRAS*, **513**, 1557  
 Casey A. R., Hogg D. W., Ness M., Rix H.-W., Ho A. Q. Y., Gilmore G., 2016, *arXiv e-prints*, p. arXiv:1603.03040  
 Castelli F., Kurucz R. L., 2003, in Piskunov N., Weiss W. W., Gray D. F., eds,

- IAU Symposium Vol. 210, Modelling of Stellar Atmospheres. p. A20 ([arXiv:astro-ph/0405087](https://arxiv.org/abs/astro-ph/0405087)), doi:10.48550/arXiv.astro-ph/0405087
- Cox D. R., 1958, *Journal of the Royal Statistical Society: Series B (Methodological)*, 20, 215
- Cropper M., et al., 2018, *A&A*, 616, A5
- Das P., Hawkins K., Jofré P., 2020, *MNRAS*, 493, 5195
- Das P. B., et al., 2025a, VizieR Online Data Catalog: Gaia RVS stellar labels using The Cannon (Das+, 2025), VizieR On-line Data Catalog: J/MNRAS/538/605. Originally published in: 2025MNRAS.538..605D
- Das P. B., et al., 2025b, *MNRAS*, 538, 605
- De Silva G. M., et al., 2015, *MNRAS*, 449, 2604
- Ernandes H., Feuillet D., Feltzing S., Skúladóttir Á., 2024, *A&A*, 691, A333
- Ernandes H., Skúladóttir Á., Feltzing S., Feuillet D., 2025, *A&A*, 703, A256
- Feuillet D. K., Feltzing S., Sahlholdt C. L., Casagrande L., 2020, *MNRAS*, 497, 109
- Feuillet D. K., Sahlholdt C. L., Feltzing S., Casagrande L., 2021, *MNRAS*, 508, 1489
- Fishlock C. K., Yong D., Karakas A. I., Alves-Brito A., Meléndez J., Nissen P. E., Kobayashi C., Casey A. R., 2017, *MNRAS*, 466, 4672
- Gaia Collaboration et al., 2016, *A&A*, 595, A1
- Gaia Collaboration et al., 2018, *A&A*, 616, A1
- Gaia Collaboration et al., 2023a, *A&A*, 674, A1
- Gaia Collaboration et al., 2023b, *A&A*, 674, A38
- Gilmore G., et al., 2012, *The Messenger*, 147, 25
- Guiglion G., et al., 2024, *A&A*, 682, A9
- Harris C. R., et al., 2020, *Nature*, 585, 357
- Hawkins K., Jofré P., Masseron T., Gilmore G., 2015, *MNRAS*, 453, 758
- Heijmans J., et al., 2012, in McLean I. S., Ramsay S. K., Takami H., eds, Society of Photo-Optical Instrumentation Engineers (SPIE) Conference Series Vol. 8446, Ground-based and Airborne Instrumentation for Astronomy IV. p. 84460W, doi:10.1117/12.925806
- Helmi A., Babusiaux C., Koppelman H. H., Massari D., Veljanoski J., Brown A. G. A., 2018, *Nature*, 563, 85
- Ho A. Y. Q., et al., 2017a, *ApJ*, 836, 5
- Ho A. Y. Q., Rix H.-W., Ness M. K., Hogg D. W., Liu C., Ting Y.-S., 2017b, *ApJ*, 841, 40
- Horta D., Ness M. K., 2025, *MNRAS*, 544, L64
- Hosmer D., Lemeshow S., Sturdivant R., 2013, *Applied Logistic Regression: Third Edition*. Wiley, doi:10.1002/9781118548387
- Hunter J. D., 2007, *Computing in Science and Engineering*, 9, 90
- Koppelman H., Helmi A., Veljanoski J., 2018, *ApJ*, 860, L11
- Koppelman H. H., Helmi A., Massari D., Price-Whelan A. M., Starkenburg T. K., 2019, *A&A*, 631, L9
- Lewis I. J., et al., 2002, *MNRAS*, 333, 279
- Luo A.-L., et al., 2015, *Research in Astronomy and Astrophysics*, 15, 1095
- Majewski S. R., et al., 2017, *AJ*, 154, 94
- Manea C., Hawkins K., Ness M. K., Buder S., Martell S. L., Zucker D. B., 2024, *ApJ*, 972, 69
- Martell S. L., et al., 2017, *MNRAS*, 465, 3203
- McKenzie M., et al., 2022, *MNRAS*, 516, 3515
- McKinney W., 2010, in SciPy. <https://api.semanticscholar.org/CorpusID:13156234>
- Monty S., Yong D., Marino A. F., Karakas A. I., McKenzie M., Grundahl F., Mura-Guzmán A., 2023, *MNRAS*, 518, 965
- Naidu R. P., Conroy C., Bonaca A., Johnson B. D., Ting Y.-S., Caldwell N., Zaritsky D., Cargile P. A., 2020, *ApJ*, 901, 48
- Naidu R. P., et al., 2021, *ApJ*, 923, 92
- Nandakumar G., et al., 2022, *MNRAS*, 513, 232
- Ness M., Hogg D. W., Rix H.-W., Ho A. Y. Q., Zasowski G., 2015, *ApJ*, 808, 16
- Nissen P. E., Schuster W. J., 2010, *A&A*, 511, L10
- Phan D., Pradhan N., Jankowiak M., 2019, *arXiv e-prints*, p. arXiv:1912.11554
- Placco V. M., Sneden C., Roederer I. U., Lawler J. E., Den Hartog E. A., Hejazi N., Maas Z., Bernath P., 2021, *Research Notes of the American Astronomical Society*, 5, 92
- Randich S., Gilmore G., Gaia-ESO Consortium 2013, *The Messenger*, 154, 47
- Recio-Blanco A., et al., 2016, *A&A*, 585, A93
- Recio-Blanco A., et al., 2023, *A&A*, 674, A29
- Sharma S., et al., 2018, *MNRAS*, 473, 2004
- Sharma S., et al., 2019, *MNRAS*, 490, 5335
- Sheinis A., et al., 2015, *Journal of Astronomical Telescopes, Instruments, and Systems*, 1, 035002
- Skúladóttir Á., Ernandes H., Feuillet D. K., Mori A., Feltzing S., Lucchesi R. E. R., Di Matteo P., 2025, *ApJ*, 986, L21
- Sneden C., 1973, *ApJ*, 184, 839
- Sneden C., Cowan J. J., Gallino R., 2008, *ARA&A*, 46, 241
- Snellen I. A. G., de Kok R. J., de Mooij E. J. W., Albrecht S., 2010, *Nature*, 465, 1049
- Taylor M. B., 2005, in Shopbell P., Britton M., Ebert R., eds, *Astronomical Society of the Pacific Conference Series Vol. 347, Astronomical Data Analysis Software and Systems XIV*. p. 29
- Taylor M., 2011, TOPCAT: Tool for OPerations on Catalogues And Tables, Astrophysics Source Code Library, record ascl:1101.010 (ascl:1101.010)
- Wheeler A., et al., 2020, *ApJ*, 898, 58

## APPENDIX A: TABLE DESCRIPTION OF *The Cannon* CATALOGUES FOR THE *Gaia*-RVS STARS

Table A1 provides the full column schema of the catalogue produced in this work. The catalogue includes *Gaia* DR3 source identifiers, equatorial coordinates (RA and Dec) and parallaxes, RVS spectral SNR, *The Cannon*-predicted stellar labels and their corresponding uncertainties, and the quality flags `fFlag_cannon` and `fFlag_XFe`, which indicate the reliability of the inferred stellar labels and individual elemental abundances, respectively, where  $X \in \{\text{Ca, Ti, Si, Ni, Nd, Ce, Zr}\}$ . The inferred labels comprise  $T_{\text{eff}}$ ,  $\log g$ ,  $\nu \sin i$ ,  $[\text{Fe}/\text{H}]$ ,  $[\text{Ti}/\text{Fe}]$ ,  $[\text{Si}/\text{Fe}]$ ,  $[\text{Ca}/\text{Fe}]$ ,  $[\text{Ni}/\text{Fe}]$ ,  $[\text{Nd}/\text{Fe}]$ ,  $[\text{Ce}/\text{Fe}]$ , and  $[\text{Zr}/\text{Fe}]$ . All abundances are reported in standard logarithmic notation relative to solar values, in units of dex. The reduced- $\chi^2$  statistic (`r_chi_sq`), quantifies the goodness of fit between the *The Cannon*-predicted spectrum and the corresponding *Gaia*-RVS spectrum for each star. In this analysis,  $\nu \sin i$  is included primarily as an additional label to improve the spectral modelling, and negative inferred values should therefore be interpreted as consistent with  $\nu \sin i = 0$ .

For scientific analyses, we recommend selecting sources with `fFlag_cannon = 0`. For studies involving individual elemental abundances, we also recommend applying the corresponding element-specific quality criterion, `fFlag_XFe = 0`. Further sample refinement may be performed by referring to Fig. C1, which shows the expected label uncertainties as a function of RVS spectral SNR.

Table A2 lists the schema of GSE membership probabilities for stars in our catalogue and their corresponding orbital parameters. The column `Prob_GSE` gives the probability ( $P_{\text{mem}}$ ) that a star is chemically similar to the *Gaia*-Sausage-Enceladus (GSE) population using the MCMC model developed on *The Cannon*-predicted chemical abundances. The kinematic quantities include the total orbital energy ( $E$ ), the Cartesian components of angular momentum ( $L_x$ ,  $L_y$ ,  $L_z$ ), the square root of the radial action ( $\sqrt{J_R}$ ), galactocentric velocities ( $V_R$ ,  $V_\phi$ ,  $V_Z$ ), and orbital eccentricity ( $e$ ), all derived from stellar orbital calculations using the MWPotential2014 Galactic potential.

Fig. A1 shows the distribution of reduced `r_chi_sq` values across the full sample of *Gaia*-RVS spectra. The reduced- $\chi^2$  statistic quantifies the goodness of fit between observed spectra and model spectra predicted by *The Cannon*; values close to unity indicate that the residual differences are broadly consistent with the estimated flux uncertainties. The distribution demonstrates that the majority of stars are fitted well by the model, indicating that *The Cannon* provides a robust representation of the observed RVS spectra across the parameter space explored in this work.

**Table A1.** Table Schema of the catalogue for *The Cannon*-estimates.

Column name	Unit	Description
Gaia_dr3_id	–	<i>Gaia</i> DR3 source ID
RA	deg	Right Ascension
e_RA	deg	Error in Right Ascension
DEC	deg	Declination
e_DEC	deg	Error in Declination
plx	mas	Parallax
e_plx	mas	Uncertainty in Parallax
rvs_snr	pix <sup>-1</sup>	<i>Gaia</i> DR3 RVS signal-to-noise ratio
flag_cannon	–	Quality flag from <i>The Cannon</i> (0/1)
Teff	K	<i>Cannon</i> -estimated effective temperature
e_Teff	K	Uncertainty in effective temperature
logg	dex	<i>Cannon</i> -estimated surface gravity
e_logg	dex	Uncertainty in surface gravity
vsini	km s <sup>-1</sup>	<i>Cannon</i> -estimated rotational velocity
e_vsini	km s <sup>-1</sup>	Uncertainty in rotational velocity
FeH	dex	<i>Cannon</i> -estimated [Fe/H]
e_FeH	dex	Uncertainty in [Fe/H]
flag_FeH	–	<i>Cannon</i> -Flag for [Fe/H] (0/1)
TiFe	dex	<i>Cannon</i> -estimated [Ti/Fe]
e_TiFe	dex	Uncertainty in [Ti/Fe]
flag_TiFe	–	<i>Cannon</i> -Flag for [Ti/Fe] (0/1)
SiFe	dex	<i>Cannon</i> -estimated [Si/Fe]
e_SiFe	dex	Uncertainty in [Si/Fe]
flag_SiFe	–	<i>Cannon</i> -Flag for [Si/Fe] (0/1)
CaFe	dex	<i>Cannon</i> -estimated [Ca/Fe]
e_CaFe	dex	Uncertainty in [Ca/Fe]
flag_CaFe	–	<i>Cannon</i> -Flag for [Ca/Fe] (0/1)
NiFe	dex	<i>Cannon</i> -estimated [Ni/Fe]
e_NiFe	dex	Uncertainty in [Ni/Fe]
flag_NiFe	–	<i>Cannon</i> -Flag for [Ni/Fe] (0/1)
ZrFe	dex	<i>Cannon</i> -estimated [Zr/Fe]
e_ZrFe	dex	Uncertainty in [Zr/Fe]
flag_ZrFe	–	<i>Cannon</i> -Flag for [Zr/Fe] (0/1)
CeFe	dex	<i>Cannon</i> -estimated [Ce/Fe]
e_CeFe	dex	Uncertainty in [Ce/Fe]
flag_CeFe	–	<i>Cannon</i> -Flag for [Ce/Fe] (0/1)
NdFe	dex	<i>Cannon</i> -estimated [Nd/Fe]
e_NdFe	dex	Uncertainty in [Nd/Fe]
flag_NdFe	–	<i>Cannon</i> -Flag for [Nd/Fe] (0/1)
r_chi_sq	–	Reduced- $\chi^2$ value

**Notes:**

- The columns Gaia\_dr3\_id, RA, e\_RA, DEC, e\_DEC, plx, e\_plx, and rvs\_snr are adopted from [Gaia Collaboration et al. \(2023a\)](#).
- flag\_X = 0 indicates that the star lies within the corresponding stellar label manifold spanned by the training sample.

**Table A2.** Table Schema of chemical similarity-based GSE membership probabilities and corresponding orbital parameters for stars in the catalogue

Column name	Unit	Description
Gaia_dr3_id	–	<i>Gaia</i> DR3 source ID
Prob_GSE	–	GSE Membership Probability ( $P_{\text{mem}}$ )
E	km <sup>2</sup> s <sup>-2</sup>	Total orbital energy ( $E$ )
Lx	kpc km s <sup>-1</sup>	Angular momentum ( $L_x$ )
Ly	kpc km s <sup>-1</sup>	Angular momentum ( $L_y$ )
Lz	kpc km s <sup>-1</sup>	Angular momentum ( $L_z$ )
sqrt_Jr	(kpc km s <sup>-1</sup> ) <sup>1/2</sup>	Square root of radial action ( $\sqrt{J_r}$ )
Vr	km s <sup>-1</sup>	Radial velocity ( $V_R$ )
Vphi	km s <sup>-1</sup>	Azimuthal velocity ( $V_\phi$ )
Vz	km s <sup>-1</sup>	Vertical velocity ( $V_z$ )
e	–	Orbital eccentricity ( $e$ )

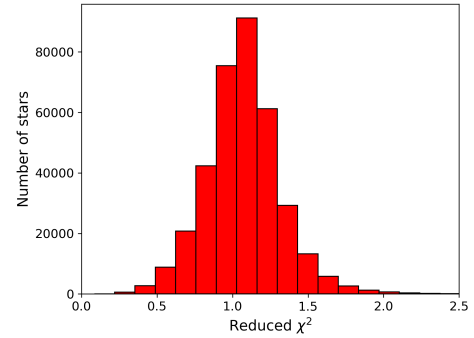
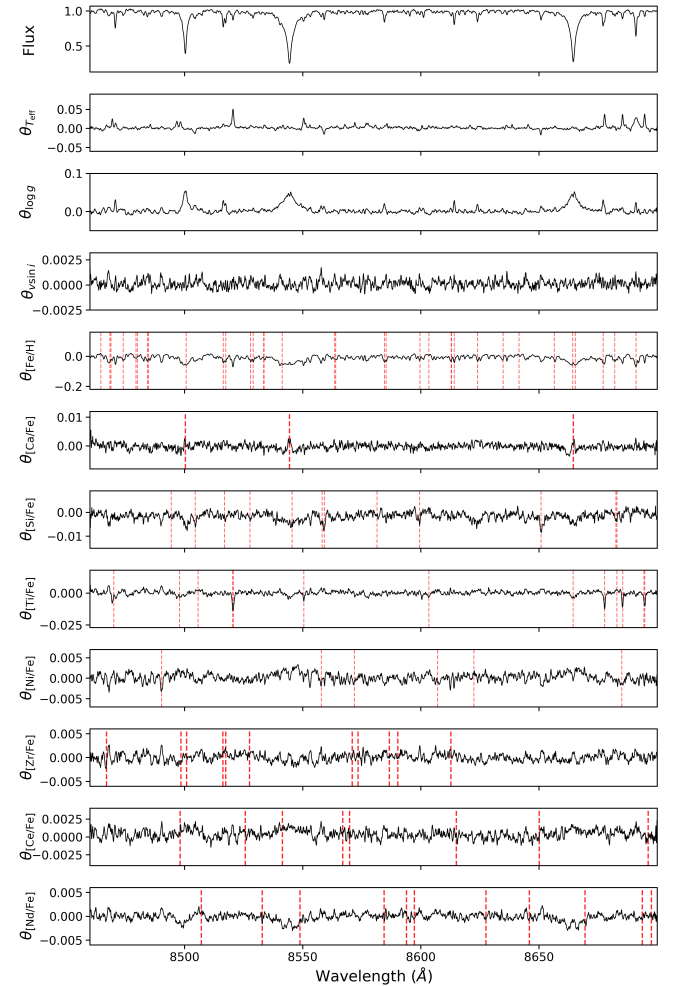
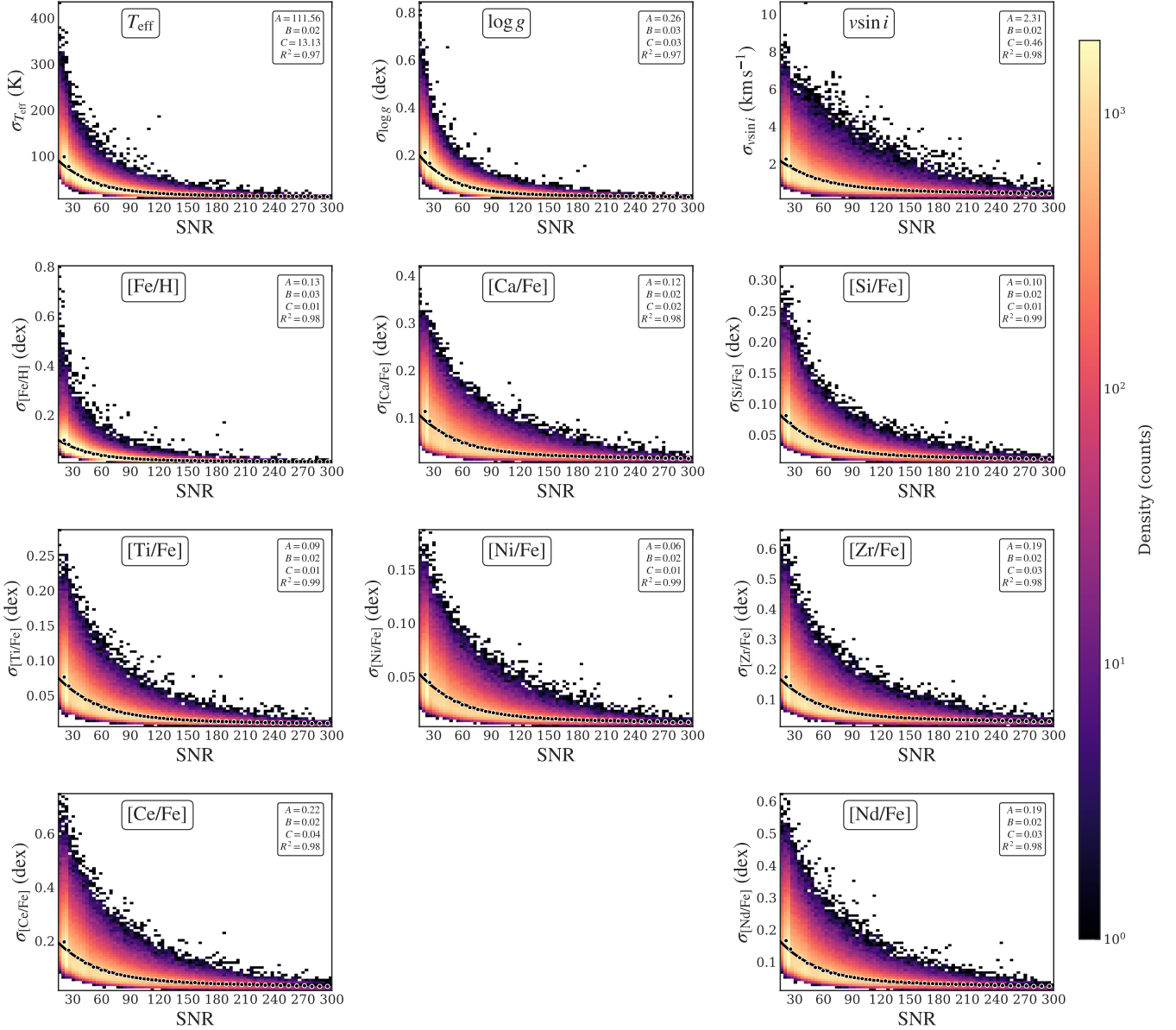
**Figure A1.** Distributions of reduced- $\chi^2$  values (r\_chi\_sq) between the predicted spectra from *The Cannon* and the corresponding observed *Gaia*-RVS spectra for all the stars in our catalogue**APPENDIX B: The Cannon MODEL COEFFICIENTS**

Fig. B1 shows the linear model coefficients for the stellar labels across the *Gaia* RVS spectral range, as inferred from modelling the training sample with *The Cannon*. These coefficients quantify the first-order sensitivity of the flux to label variations at each wavelength pixel.

**Figure B1.** The topmost panel shows the *Gaia* RVS spectrum of a randomly selected star. The lower panels show the linear model coefficients from *The Cannon* ( $\theta$ ) for the entire training sample of 2747 stars across the *Gaia* RVS spectral wavelength range for each stellar label. Red dashed vertical lines show the spectral lines associated with the corresponding abundance label.

APPENDIX C: ERROR BUDGET IN STELLAR LABELS ACROSS *Gaia*-RVS SPECTRAL SNR

To quantify the dependence of the reported label uncertainties on spectral quality, we examined the total label uncertainties as a function of the *Gaia* RVS signal-to-noise ratio (RVS SNR) for all stars in the final catalogue. Fig. C1 presents this relation for each stellar parameter and elemental abundance.



**Figure C1.** Uncertainties in the *The Cannon*-derived stellar labels as a function of *Gaia* RVS spectral SNR for the stars in the catalogue. The colour scale indicates the two-dimensional density of stars in each panel. The black curve shows a robust exponential fit of the form  $\sigma_{\text{label}} = Ae^{-(B \cdot \text{SNR})} + C$ , where  $\sigma$  denotes the reported uncertainty for each label. The fitted parameters and the coefficient of determination ( $R^2$ ) are listed in each panel. In all cases, the uncertainties decrease systematically with increasing spectral signal-to-noise ratio and asymptotically approach a precision floor at high SNR, represented by the constant term  $C$ .

In each panel, the two-dimensional density of stars is shown, and an exponential model of the form  $\sigma_{\text{label}} = Ae^{-(B \cdot \text{SNR})} + C$  is fitted to the data. Here,  $A$  characterizes the amplitude of the decrease in uncertainty toward lower signal-to-noise ratios,  $B$  determines the rate at which the uncertainties improve with increasing SNR, and  $C$  represents the asymptotic precision floor reached at high SNR. The fits were obtained using a two-stage procedure in which median uncertainties were first computed in signal-to-noise bins and subsequently modelled with an exponential function. This approach provides a stable and physically interpretable representation of the uncertainty–SNR relation across all labels.

The results show a monotonic decline in uncertainties with increasing SNR, with each label approaching a well-defined high-SNR precision limit. These empirical relations provide a practical framework for estimating the expected precision of the catalogue as a function of spectral quality and may be used to guide sample selection for applications requiring specific uncertainty thresholds.

**APPENDIX D: LINE PARAMETERS FOR Ce, Zr, and Nd**

Table D1 lists the vacuum and air wavelengths, species, excitation potentials (E.P.), and oscillator strengths ( $\log gf$ ) for the Ce, Zr, and Nd from the Atomic and Molecular Line List Generator `linemake`. These sets of lines are contained within the *Gaia*-RVS wavelength range and were used in the *pseudo*-differential abundance analysis illustrated in Fig. 4. The 3 species (Ce, Zr, and Nd), follow the standard notation where neutral species are denoted as X.0 and ionised species as X.1, with X being the atomic number.

**Table D1.** Wavelengths, species, oscillator strengths, and excitation potentials for selected lines of Ce, Zr, and Nd. This linelist was created using `linemake`.

$\lambda$ vac. (Å)	$\lambda$ air (Å)	Species	E.P. (eV)	$\log(gf)$ (dex)
Zr				
8467.013	8464.687	40.0	0.650	-2.08
8498.451	8496.117	40.0	2.124	-1.37
8500.857	8498.522	40.0	0.622	-2.22
8516.255	8513.916	40.0	0.632	-3.11
8517.387	8515.047	40.0	2.114	-1.64
8527.475	8525.133	40.1	2.408	-1.00
8570.941	8568.587	40.0	0.730	-2.80
8573.440	8571.085	40.0	1.529	-2.07
8586.639	8584.281	40.0	1.873	-1.32
8590.224	8587.865	40.0	1.481	-2.12
8612.678	8610.313	40.0	1.481	-2.27
Ce				
8498.159	8495.825	58.0	0.294	-1.65
8525.704	8523.362	58.0	0.294	-1.74
8541.447	8539.101	58.1	0.175	-3.20
8566.934	8564.581	58.0	0.274	-1.80
8569.833	8567.479	58.0	0.493	-1.51
8615.016	8612.650	58.0	0.466	-1.39
8650.030	8647.655	58.0	0.552	-1.30
8696.144	8693.756	58.1	2.279	-1.26
Nd				
8507.107	8504.770	60.1	1.356	-1.68
8532.889	8530.545	60.1	0.064	-3.61
8548.828	8546.480	60.1	2.019	-1.23
8584.472	8582.114	60.1	1.698	-1.46
8593.890	8591.530	60.1	1.357	-1.65
8597.244	8594.883	60.1	1.140	-1.86
8627.539	8625.170	60.1	1.877	-1.45
8645.854	8643.480	60.1	1.199	-1.29
8669.456	8667.075	60.1	1.263	-1.89
8693.690	8691.303	60.1	1.349	-1.73
8697.558	8695.170	60.1	1.698	-1.38

Thresholds ranging from 50% to 95% were evaluated using the validation sample of 86 GSE stars (common to our catalogue and [Feuillet et al. 2021](#)), which was used to train the MCMC-based classifier. For each threshold, we tracked the true positives (TP), false positives (FP), and false negatives (FN). As the threshold increases, precision improves (fewer false positives), recall decreases (more missed GSE stars), and the total numbers of predicted and estimated true GSE stars decline, producing a progressively more conservative sample. We adopt a threshold of 55% (highlighted in bold) for our analysis, as this value provides a balance between minimizing false positives and retaining the majority of true GSE members, yielding a representative and reliable sample for subsequent population analysis.

**Table E1.** Membership classification metrics for different probability thresholds applied to GSE candidate stars. The threshold of 55% (highlighted in bold) is adopted in our analysis, where the number of false positives is controlled while retaining the majority of true GSE members.

Threshold (%)	TP	FP	FN	Precision (%)	Recall (%)	Predicted GSEs	Estimated True GSEs
50	53	27	33	66.25	61.63	3595	2382
<b>55</b>	<b>50</b>	<b>22</b>	<b>36</b>	<b>69.44</b>	<b>58.14</b>	<b>3295</b>	<b>2289</b>
60	45	20	41	69.23	52.33	3042	2106
65	44	18	42	70.97	51.16	2769	1966
70	37	14	49	72.55	43.02	2481	1800
75	30	12	56	71.43	34.88	2235	1597
80	27	9	59	75.00	31.40	1985	1489
85	25	5	61	83.33	29.07	1705	1421
90	18	4	68	81.82	20.93	1364	1117
95	12	3	74	80.00	13.95	914	732

**Notes:**

- *Threshold* – Adopted membership probability threshold.
- *TP* – Number of true positives correctly identified in the validation sample of 86 confirmed GSE stars.
- *FP* – Number of false positives, i.e. stars incorrectly classified as GSE members.
- *FN* – Number of false negatives, i.e. GSE stars missed by the classification.
- *Precision* – Fraction of predicted GSE members that are truly GSE, calculated as  $TP/(TP + FP)$ .
- *Recall* – Fraction of true GSE stars correctly identified, calculated as  $TP/(TP + FN)$ .
- *Predicted GSEs* – Total number of probable GSE candidates satisfying  $P_{\text{mem}} > \text{Threshold}$ .
- *Estimated True GSEs* – Estimated true number of GSE stars, obtained by multiplying the precision by the number of predicted GSE candidates.

**APPENDIX E: GSE-MEMBERSHIP PROBABILITY THRESHOLD SELECTION**

Table E1 summarizes the classification metrics for different membership probability thresholds applied to the GSE candidate stars.

## APPENDIX F: CHEMICAL PROFILE OF PROBABLE GSE CANDIDATE MEMBERS

Fig. F1 shows the distribution of all possible pairwise chemical abundance ratios constructed from the elements [Fe, Ca, Ti, Nd, Zr, Ce] for the 2289 high-confidence probable GSE candidates ( $P_{\text{mem}} > 55\%$ ). These distributions are compared against those of Milky Way halo and thick disc stellar populations, as well as a reference sample of 86 stars common to our catalogue and the GSE sample from Feuillet et al. (2021).

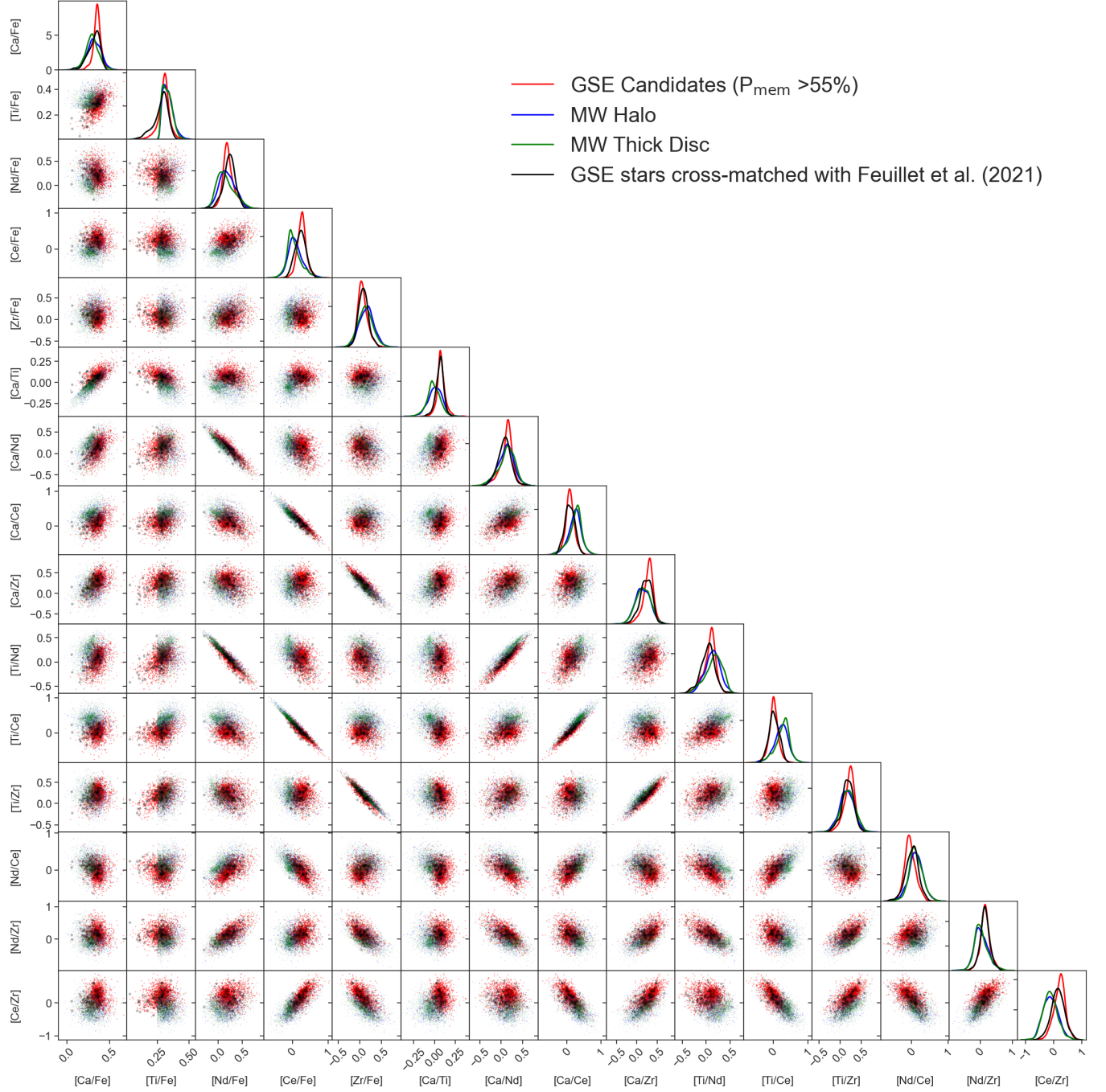


**Figure F1.** Distributions and pairwise correlations of elemental abundance ratios involving Fe, Ca, Ti, Nd, Ce, and Zr for four stellar populations: 2289 predicted GSE candidate stars with  $P_{\text{mem}} > 55\%$  (red), kinematically selected halo stars (blue), thick disc stars (green), and a crossmatch of 86 GSE stars from Feuillet et al. (2021) with our catalogue of 314,010 *Gaia*-RVS stars (black) satisfying `flag_cannon = 0`. One-dimensional kernel density estimates are shown on the diagonal, and two-dimensional scatter plots appear below the diagonal. The distinct abundance trends, particularly in neutron-capture and  $\alpha$ -element ratios such as [Ca/Ti], [Ti/Ce], and [Nd/Zr], reveal clear chemical differentiation between the accreted GSE and *in situ* populations, highlighting their utility as tracers of stellar origin in the Milky Way.